



United States Department of Commerce
Technology Administration
National Institute of Standards and Technology

NIST Technical Note 1366

Analytical Estimation of Carrier Multipath Bias on GPS Position Measurements

**C. Michael Volk
Judah Levine**

QC
100
.U5753
#1366
1994

Analytical Estimation of Carrier Multipath Bias on GPS Position Measurements

**C. Michael Volk
Judah Levine**

Time and Frequency Division
Physics Laboratory
National Institute of Standards and Technology
325 Broadway
Boulder, Colorado 80303-3328

April 1994



**U.S. DEPARTMENT OF COMMERCE, Ronald H. Brown, Secretary
TECHNOLOGY ADMINISTRATION, Mary L. Good, Under Secretary for Technology
NATIONAL INSTITUTE OF STANDARDS AND TECHNOLOGY, Arati Prabhakar, Director**

National Institute of Standards and Technology Technical Note
Natl. Inst. Stand. Technol., Tech. Note 1366, 68 pages (April 1994)
CODEN:NTNOEF

U.S. GOVERNMENT PRINTING OFFICE
WASHINGTON: 1994

For sale by the Superintendent of Documents, U.S. Government Printing Office, Washington, DC 20402-9325

CONTENTS

CHAPTER

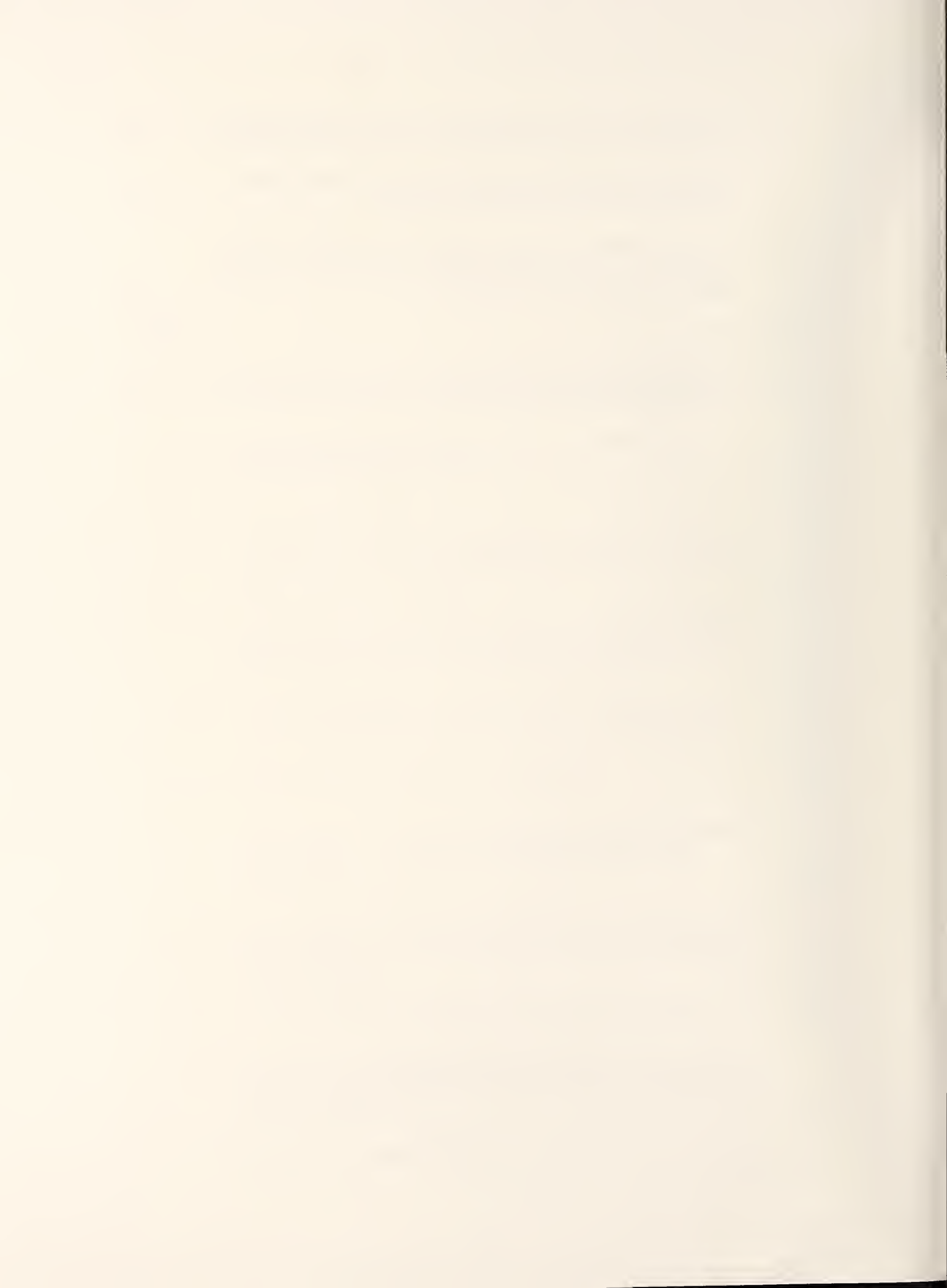
1.	INTRODUCTION	2
1.1	Brief Introduction to GPS	3
1.2	The GPS Experiment "EDM"	4
1.3	Multipath Signatures in GPS Data	7
2.	GENERAL APPROACH	9
2.1	The Multipath Error Phase	9
2.2	Position Bias Resulting from Phase Error	13
2.2.1	The Least Squares Adjustment	13
2.2.2	Parameterization for Analytical Treatment	15
2.3	Generic Calculation for Azimuthal Symmetry	17
2.3.1	Reducing to the Case of Azimuthal Symmetry	17
2.3.2	Numerical Integration	20
2.3.3	Approximating the Elevation Integrals	20
2.4	Generalization to Dual Frequency Observations	26
3.	CALCULATIONS FOR SIMPLE REFLECTOR GEOMETRIES	31
3.1	Outline of the Strategy	31
3.2	Multipath from Flat Ground	33
3.2.1	Full Azimuthal Symmetry	33
3.2.2	Disturbed Symmetry	34
3.3	Multipath from Nearby Objects	35
3.4	Multipath from Tilted Ground	39
4.	APPLICATION OF THE MODEL	43
4.1	Limitations of the Applicability	43
4.1.1	Non-uniform Satellite Distribution	44
4.1.2	Other Unmodelled Effects	47
4.2	Estimating the Amplitudes	48
4.3	Position Bias at "nist"	50
4.4	Position Bias at "eri1"	52
5.	SUMMARY AND CONCLUSIONS	54
	REFERENCES	59

FIGURES

Figure

1.1	Horizontal components of the baselines nistrfcr and platrfcr in four processing runs with varying minimum satellite elevation h_{\min}	6
1.2	L3 (upper plot) and L4 (lower plot) postfit double-difference residuals of the baseline nistrfcr	8
2.1	General geometry and variable definitions used in this chapter.....	10
2.2	Multipath error phase M versus satellite angle above the reflector plane h' for relative multipath amplitudes (a) $A \rightarrow 1$ and (b) $A = 0.5$	12
2.3	Multipath error phase contours as function of satellite elevation h above the horizon and azimuth a as seen from the receiver for a reflector surface tilted 45° with respect to the horizon	19
2.4	Numerical integration of the integrals (a) $I_{0xy} = I_{xy}(h_{\min}=0)$ and (b) $I_{0z} = I_{xy}(h_{\min}=0)$ as functions of upper integration limit h_{\max}	21
2.5	$M(x)$ normalized to amplitude 1 for varying A's	22
2.6	Exact integrals (black lines) and approximated integrals (gray lines): (a) I_{0xy} and \tilde{I}_{0xy} , (b) I_{0z} and \tilde{I}_{0z} as functions of their upper integration limit h_{\max}	26
2.7	Exact integrals (black lines) and approximated integrals (gray lines): (a) I_{30xy} and \tilde{I}_{30xy} , (b) I_{30z} and \tilde{I}_{30z} as functions of their upper integration limit h_{\max}	29
3.1	Asymmetrical multipath region for flat ground as reflector.....	34
3.2	Multipath from a nearby planar reflector parallel to the y-axis, horizontally symmetrical with respect to the x-axis, and at an angle α from the horizon.....	36
3.3	Multipath from a vertical reflector	38

3.4	Multipath from the ground tilted at an angle α from the horizon	40
4.1	Satellite elevations (upper plot) and azimuths (lower plot) in degrees as functions of time for station rfc1	45
4.2	L3 postfit double difference residuals for the baselines nister1 (upper plot) and eri2eri1 (lower plot) at day 078 (the first day of the “EDM” experiment).....	49
4.3	Geometry at the receiver site nist	51
4.4	Geometry at the receiver site eri1.....	52



Analytical Estimation of Carrier Multipath Bias on GPS Position Measurements

C. Michael Volk*

Joint Institute for Laboratory Astrophysics
University of Colorado
Boulder, Colorado 80309

and

Judah Levine**

Time and Frequency Division
National Institute of Standards and Technology
Boulder, Colorado 80303

Multipath is one of the factors degrading the accuracy of position measurements obtained with the Global Positioning System (GPS). We investigate the effects of multipath on the carrier phase measurement and the resulting bias on relative GPS positions for observation times longer than several hours.

A short-range GPS network was surveyed with day-long observation sessions. The data display obvious multipath signatures and the position results indicate the presence of site-specific errors at the level of several millimeters. This led us to suspect multipath bias and motivated the quantitative estimation presented here. We first model the phase error due to multipath from a single plane reflector in terms of satellite-reflector geometry. The effect of this error on position is then derived by performing a simplified least squares adjustment under the assumption of uniform satellite distribution. After several steps of approximations and manipulations we arrive at simple expressions for the bias in terms of general receiver-reflector geometry and a few other variables. The results are generalized to dual frequency observations that are commonly used for high accuracy observations.

The model is then employed to estimate upper limits of the multipath bias for general receiver environments. We consider bias due to multipath from the flat ground, from nearby objects, and from a tilted ground, obtaining formulae for each situation that depend only on reflector characteristics and geometry. Finally, these results are applied to the GPS experiment. Limitations of the applicability due to model assumptions and unmodelled effects are discussed. The two stations thought to be most affected by multipath in the experiment are examined. We find that the multipath phase error as inferred from the observations can give rise only to vertical biases smaller than 2 mm and horizontal biases smaller than 1 mm. It is thus concluded that bias due to multipath-induced carrier phase error is effectively reduced by averaging if observation intervals are at least several hours long and some basic precautions are taken regarding the receiver environment.

Keywords: GPS geodesy; GPS measurements; multipath bias

* Current affiliation: Cooperative Institute for Research in Environmental Sciences and Department of Physics, University of Colorado, Boulder, CO 80309.

**Fellow, Joint Institute for Laboratory Astrophysics, University of Colorado, Boulder, CO 80309.

CHAPTER 1

INTRODUCTION

“Multipath” has long been recognized as a significant error source in high accuracy applications of the Navigation Satellite Timing and Ranging (NAVSTAR) Global Positioning System (GPS). It occurs when a satellite signal is reflected from objects in the vicinity of the receiver causing multiple arrivals of the same signal. Interference of these arrivals corrupts the “true” (direct) signal with time-dependent signatures. Many studies on multipath have focused on how to detect and reduce it (e.g., [1]). Considerable effort has been undertaken to design antennas and backplane configurations that minimize the sensitivity of the receiver’s antenna in the direction of reflectors at low elevation angles [2,3].

Because multipath signatures on the carrier phase tend to oscillate with periods shorter than 10 to 20 min, it is clear that their effect is most serious for GPS applications with short observing sessions and for kinematic applications. Several authors have stated that observations over several hours are likely to average out most of the effect on relative positioning [4,5,6].

This work developed out of a continuous discussion about how big the net bias on relative positions due to multipath could be in a recent GPS experiment using observation sessions of 23 h. The experiment and some results hinting at multipath problems are discussed later in this chapter; preceding is an (ultra-)brief introduction to GPS. The main part of this report is of a rather theoretical nature: In Chapter 2 we develop the mathematical frame and tools. These are used in the third chapter to estimate the multipath-induced bias for several simple reflector-receiver geometries. Chapter 4 attempts to quantify the analysis and to apply the results to two receiver sites of the GPS experiment mentioned above. Conclusions are drawn in the final fifth chapter.

1.1 Brief Introduction to GPS

GPS satellites orbiting at 20,000 km altitude transmit two carrier radio signals L1 and L2 at frequencies of about 1.23 and 1.58 GHz (wavelengths of about 19 and 24 cm). These are modulated with lower frequency codes, most importantly the pseudo-random P-code at 10.23 MHz. The codes are used to simultaneously measure the time delay of signals from several satellites at the receiver (“pseudorange measurement”). An instantaneous receiver position with meter accuracy is thus obtained, e.g., for navigational applications (the original purpose of GPS). Even before the system was operational, the potential use of the carrier signals for precise relative positioning was realized and several methods were suggested on how to extract vector baselines at centimeter-level accuracy [7].

In principle, the phase from at least two satellites (usually more than four) is measured at two (or more) receivers simultaneously, thus eliminating systematic receiver and satellite clock offsets by common mode cancellation. The simultaneous phases of each pair of receivers and each pair of satellites are subtracted from each other to arrive at “double difference” observations. The double differenced satellite ranges are ambiguous by an unknown number of carrier wavelengths and left with errors due to differential propagation delays. The latter are corrected by various methods. Since the ionosphere is dispersive in the radio band, dual frequency observations (L1 and L2) allow elimination of major ionospheric effects. The ionosphere corrected range is an appropriate linear combination of L1 and L2 called L3. The non-dispersive atmospheric delay (mainly due to the troposphere) must be corrected by modelling using surface measurements. This method works well for the dry air which is approximately in hydrostatic equilibrium, but is less satisfactory for the water vapor contribution. Often water vapor radiometers are used to measure the wet delay; sometimes stochastic estimation techniques are invoked. There is some argument as to which method produces better results [8].

If the differenced satellite ranges are tracked while maintaining lock with the signal, the baseline vector can be obtained provided that the satellite orbits and the initial cycle ambiguities (or “phase biases”) are known. Nowadays the orbits are determined by continuously tracking the satellites from a continental-sized or even global network of “fiducial stations” whose coordinates are well known from other techniques (VLBI or SLR). The phase ambiguities and relative station positions are then solved for using a least-squares adjustment of all observations starting from a priori coordinates that are usually known to within a few centimeters from pseudorange measurements. For

baselines shorter than 100 km most of the cycle ambiguities can usually be constrained to their integer values. In a repeated adjustment the known ambiguities are constants and only the station coordinates are estimated (usually relative to one fixed station). It is actually not required that the ambiguities be fixed to integers since the best fitting real numbers determined by the least squares adjustment are sufficient to yield meaningful position results. However, the precision of the measurement increases if the biases can be fixed. A comprehensive discussion of the fundamentals of GPS has been given by Rocken [9].

Most errors affecting GPS relative positioning are proportional to the baseline length, e.g., orbit errors, atmospheric path delay errors, errors in the absolute position of the fixed station (e.g., [10]). Besides receiver setup errors, the dominant length-independent error sources are multipath and two even more complex phenomena, antenna phase center variations and imaging [11]. The latter of these two effects is related to multipath and is difficult to distinguish from it. Phase center variations and imaging will be ignored in this work, yet it ought to be kept in mind that they may be non-negligible.

1.2 The GPS Experiment “EDM”

A GPS experiment titled “EDM” was conducted in cooperation with the University NAVSTAR Consortium (UNAVCO), Boulder, in March 1993. The objective was to compare distances measured by GPS and the JILA three-wavelength electromagnetic distance-measuring (EDM) instrument [12]. We had been testing the latter system during several months in a two-wavelength mode over a baseline between the top of a mesa west of the NIST facilities in Boulder and the base of a meteorological tower operated by NOAA near Erie, Colorado. The EDM yielded a precision of better than 2 mm over this distance of 24 km, i.e., better than 0.1 ppm.

The GPS data were acquired at a sampling rate of 15 seconds during 3 daily sessions each lasting 23 h starting at GPS time 17:00 on March 19, 20, and 21, respectively. Four sites were occupied with *Trimble 4000 SST* dual-frequency receivers: the two benchmarks at the NIST mesa (“nist”) and at the tower base at Erie (“eri1”) used for the EDM tests; another benchmark on NOAA land some 200 m from eri1 (“eri2”); and a benchmark on top of the UNAVCO building in Boulder (“rfcr”). A fifth receiver at Platteville, Colorado (“plat”) is operated permanently by UNAVCO and served as a reference position. The receivers at rfcr and plat were hard-mounted, whereas nist, eri1, and eri2 were subject to a daily setup error.

The data were then processed with the Bernese 3.3 software that uses double difference observables in one least squares adjustment in the way described above. In general, more than 95 percent of the ambiguities for any given baseline and day could be fixed to their integer values. Initially, baselines from nist to eri1, eri2, and rfc1 were included in a series of processing runs under varying processing parameters. The results showed good agreement between the distances on the first and third day but a consistent 3 to 5 mm increase in the nist-to-eri baselines for the second day mainly due to an apparent offset of nist to the west. In a second series of runs we processed baselines from rfc1 to all other stations, including plat, in order to discriminate between potential error sources. Surprisingly, the longest baseline of 47 km from rfc1 to plat (“platrfc1”) showed the best horizontal repeatability over the three days while horizontal scatter in the distance from rfc1 to nist (“nistrfc1”) was biggest, up to 4 mm peak-to-peak. Consequently, the main contributing error sources must be length-independent. In fact, baseline nistrfc1 is so short (5.5 km) that scale errors should be negligible altogether.

In order to investigate if the unexpected high scatter in the horizontal components of nistrfc1 was likely to be due to setup errors at nist, we split up the data into three (approximately) 8-h sessions for each day. Figure 1.1 shows the “time series” of the resulting nine sessions for four processing runs in which the minimum satellite elevation above the horizon (“ h_{\min} ”) was varied from 20° to 35° . It can be seen that: (i) the scatter in nistrfc1 is as big or bigger as in platrfc1; (ii) scatter within one day is not smaller than scatter between days (which would have been expected for setup errors); and (iii) that the minimum satellite elevation has quite an influence on the result, in particular for baseline nistrfc1.

We thus arrive at the conclusion that site-specific problems giving rise to systematic bias of the position are likely to be present at nist. Multipath is one of the prime candidates for such problems. While these results certainly motivated the discussion that led to this work, they should by no means be considered as proof for the “multipath case”.

Several ambiguous and unexplained factors not mentioned so far remain:

- The site most suffering from multipath is clearly eri1. As will be discussed in Chapter 4, this benchmark is surrounded by nearby trailers and the noise in the post-fit double difference residuals is about twice that of all other baselines. However, this is not apparent in the position results. In fact, the two Erie sites consistently yield results very similar to each other in all the processing runs and there is no evidence for site-dependent bias at eri1.

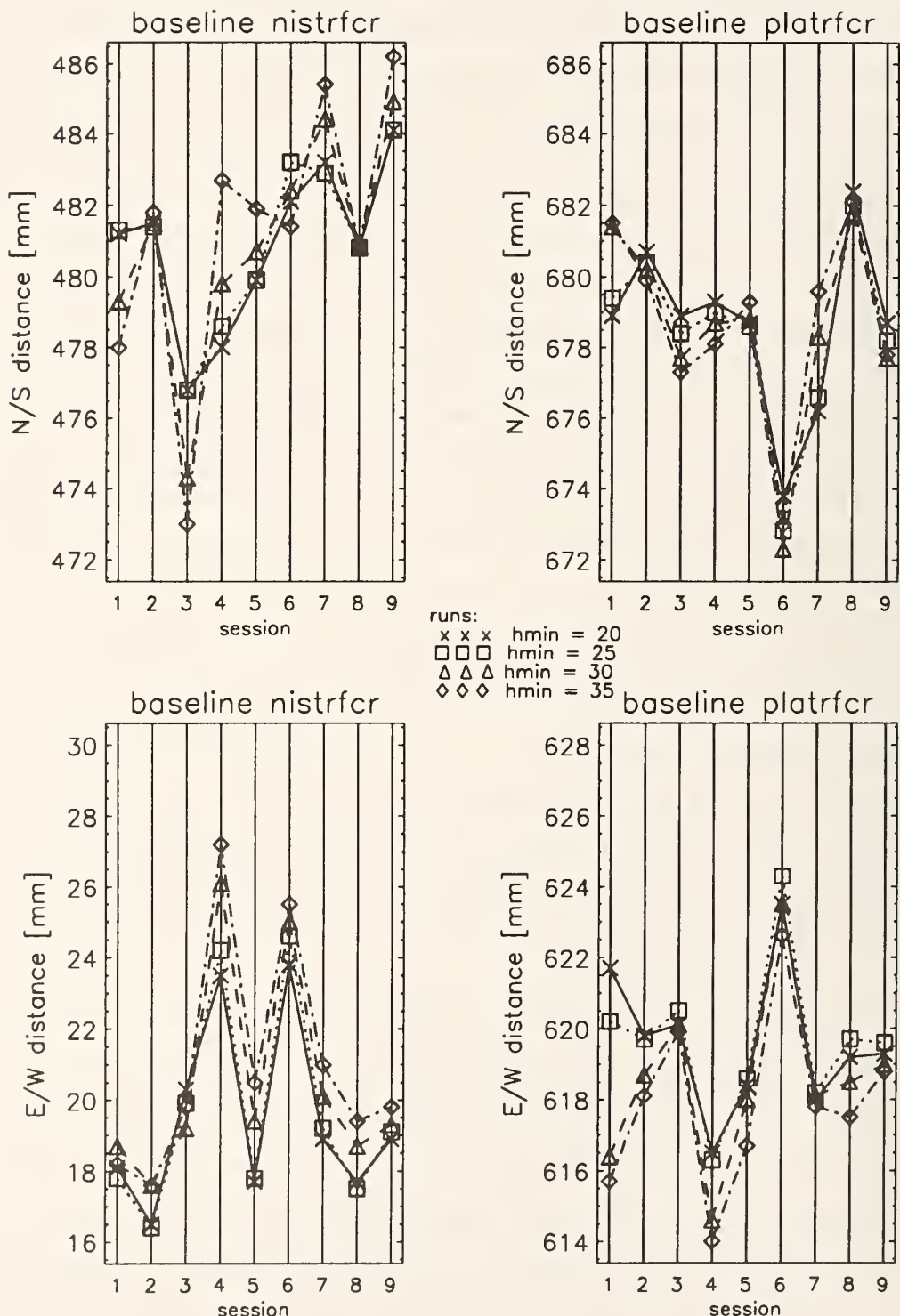


Figure 1.1. Horizontal components of the baselines nistrfcr and platrfcr in four processing runs with varying minimum satellite elevation h_{\min} . Sessions are approximately 8 h. The setup at nist was changed daily, i.e., after sessions 3 and 6, but remained unchanged at rfc and plat.

- Judging from the noise in the double difference post-fit residuals, nist is no worse than any of the other sites.
- There were, however, mysterious receiver outages reoccurring daily at nist around 0:00 GPS time. The resulting gaps of up to one hour in the data caused unexplained problems in the processing. Special data editing during preprocessing was required to arrive at meaningful results at all.

No attempt is made in this work to further investigate any of these points. Instead of trying to find out just what the problem at nist is, we will content ourselves with estimating how much of a problem multipath could be in the given environment.

1.3 Multipath Signatures in GPS Data

Phase multipath is relatively easy to detect if dual frequency observations are available. Other noise sources that can leave similar signatures in the data are highly time-variable ionosphere noise, tropospheric delay errors, and different sorts of geometric errors (satellite and receiver positions, clock errors). Ionospheric delay is eliminated in the ionosphere-free linear combination L3 (section 1.1) while geometric errors and tropospheric effects are common to both frequencies and thus cancelled by forming the “geometry-free” linear combination $L4 = L1 - L2$. L4 is simply the differential range of L1 and L2 that is due to the ionosphere and other effects not common to both frequencies like multipath.

As pointed out by Rocken [9], any correlation between L3 and L4 post-fit residuals must be due to measurement noise (3 mm) or multipath and related effects (imaging, phase center variations). Hence, a simple inspection by eye will usually reveal multipath signatures. An example from the baseline nistrfcr is given in figure 1.2. Another indicator for multipath is noise signatures that repeat from day to day. Because the satellite-receiver geometry repeats daily (shifted by 4 min), the multipath does, too. This was evident in nearly all of the experimental data from the “EDM” campaign. Indeed, we made use of the repetitive nature of multipath during data editing to distinguish cycle slips (which would not repeat daily) from high frequency high amplitude multipath noise. This was especially helpful for baselines including eri1 where the program in automatic mode frequently mistook “jumps” in the residuals caused by multipath as cycle slips.

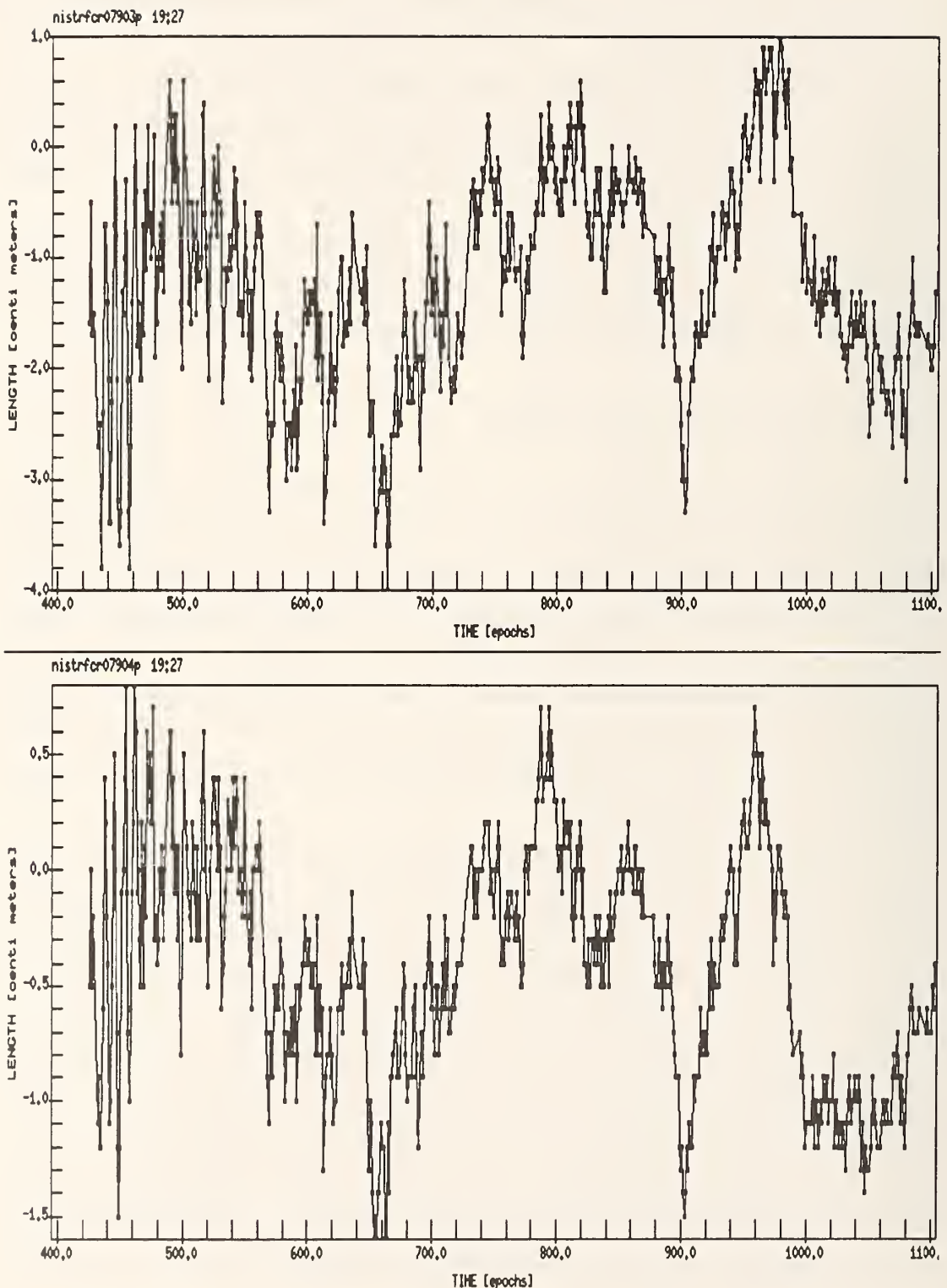


Figure 1.2. L3 (upper plot) and L4 (lower plot) postfit double-difference residuals of the baseline nistrfcr. Any correlation between the two plots is due to multipath.

CHAPTER 2

GENERAL APPROACH

The goal of this chapter is to express the bias of GPS derived positions resulting from multipath in terms of receiver-reflector geometry and a few other variables. We start out by modelling the multipath error phase in terms of geometry. In a second step we derive the position bias due to this error phase. The analytical expressions thus found will then be approximated in order to simplify the calculations for a given environment. The discussion will be restricted to a single planar reflector.

2.1 The Multipath Error Phase

Consider a signal from a satellite that arrives at a receiver R via two different paths: the direct path and the multipath due to reflection from a nearby planar object. This causes the arrival of two signals at the receiver which are out of phase because the two paths have different lengths. We start out by calculating the pathlength difference between the two paths. For a plane reflector at a perpendicular distance d from the receiver the length of the multipath is equivalent to the length of a path from the satellite to a (stationary) image receiver R' an equal perpendicular distance behind the reflecting surface. The general geometry and variables used in the following are introduced in figure 2.1.

As s and s' are essentially parallel, the pathlength difference Δs is simply the length of $R'R = 2dn$ projected on s' :

$$\Delta s = 2dn \cdot \hat{s}' \equiv 2dn \cdot \hat{s} \quad (2.1)$$

where \hat{s} is the unit vector in direction of s . If λ is the wavelength of the signal, then the resulting phase difference between the direct and the multipath signal is

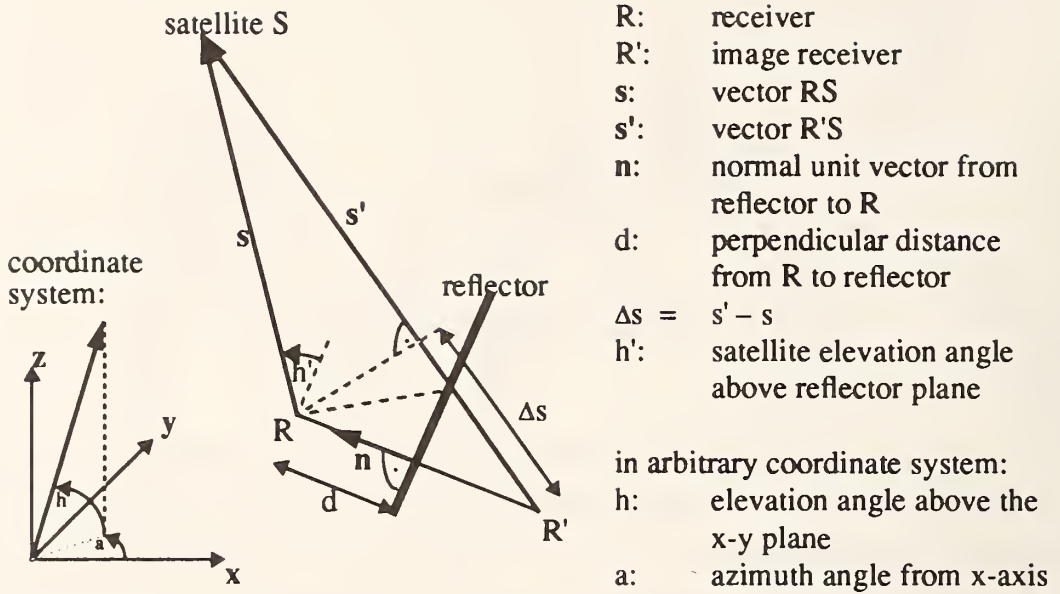


Figure 2.1. General geometry and variable definitions used in this chapter.

$$\Delta\phi = \frac{2\pi}{\lambda}\Delta s = \frac{4\pi d}{\lambda} \mathbf{n} \cdot \hat{\mathbf{s}}. \quad (2.2)$$

The two signals arriving at the receiver are

$$S_{\text{direct}} = A_1 \sin(\omega t) \quad \text{and} \quad S_{\text{multi}} = A_2 \sin(\omega t + \Delta\phi),$$

$\omega = 2\pi c/\lambda$ being the angular frequency of the satellite signal. They combine at the receiver phase center yielding the total signal:

$$S_{\text{total}} = A_1 \sin(\omega t) + A_2 \sin(\omega t + \Delta\phi). \quad (2.3)$$

This can be expressed as $S_{\text{total}} = A_{\text{total}} \sin(\omega t + M)$, where

$$A_{\text{total}} = \sqrt{A_1^2 + A_2^2 + 2A_1 A_2 \cos \Delta\phi} \quad (2.4)$$

and

$$\tan M = \frac{A_2 \sin \Delta\phi}{A_1 + A_2 \cos \Delta\phi}. \quad (2.5)$$

With the relative multipath signal amplitude $A \equiv A_2/A_1 \leq 1$ we thus arrive at an expression for the error phase due to multipath,

$$M = \text{atan} \left[\frac{\sin \left(\frac{4\pi d}{\lambda} \mathbf{n} \cdot \hat{\mathbf{s}} \right)}{A^{-1} + \cos \left(\frac{4\pi d}{\lambda} \mathbf{n} \cdot \hat{\mathbf{s}} \right)} \right] . \quad (2.6)$$

M has the following features:

- For the special case $A = 1$ the right hand side of eq (2.5) becomes $\tan(\Delta\phi/2)$ and thus $M = \Delta\phi/2$. Because of equal amplitudes, signals S_{direc} and S_{multi} are indistinguishable resulting in a phase of S_{total} equal to the average of their phases, $\omega t + \Delta\phi/2$. This case is obviously of no practical relevance.
- For $A < 1$ M is amplitude limited: $|M| \leq \pi/2$ or smaller than a quarter of a cycle. The maximum amplitude of M is determined exclusively by A .
- As the satellite moves, M undergoes cyclic variations. The periodicity of M is the same as that of the sine in the numerator of eq (2.6), i.e., it oscillates with an angular frequency $\frac{d}{dt} \Delta\phi$.
- It follows from eq (2.2) that the multipath oscillation frequency is proportional to d/λ and to

$$\frac{d}{dt} (\mathbf{n} \cdot \hat{\mathbf{s}}) = \frac{d}{dt} \sinh' = \cosh' \cdot \frac{d}{dt} h',$$

i.e., it increases with the distance to the reflector, decreases for longer wavelengths, and increases with the rate of change and the cosine of the satellite elevation angle h' above the reflector plane.

A derivation similar to the preceding one has been given by Georgiadou and Kleusberg [5]. They obtain an oscillation period of 3.2 min for $h' = 45^\circ$, $d = 10$ m, and an average rate of change of the satellite elevation angle. This number is within the typical range of oscillation periods evident in experimental GPS data.

Figure 2.2 shows M as a function of h' for $A \rightarrow 1$ and for $A = 0.5$. In the case $A = 1$ M would simply be wrapped, i.e., instead of the jumps of $-1/2$ cycles visible in figure 2.1a, the sections would be appended one to the next to give a smooth function. For small A , M becomes more harmonic. Changing λ or d would have no influence on the shape of M , but simply change the scale on the h' axis.

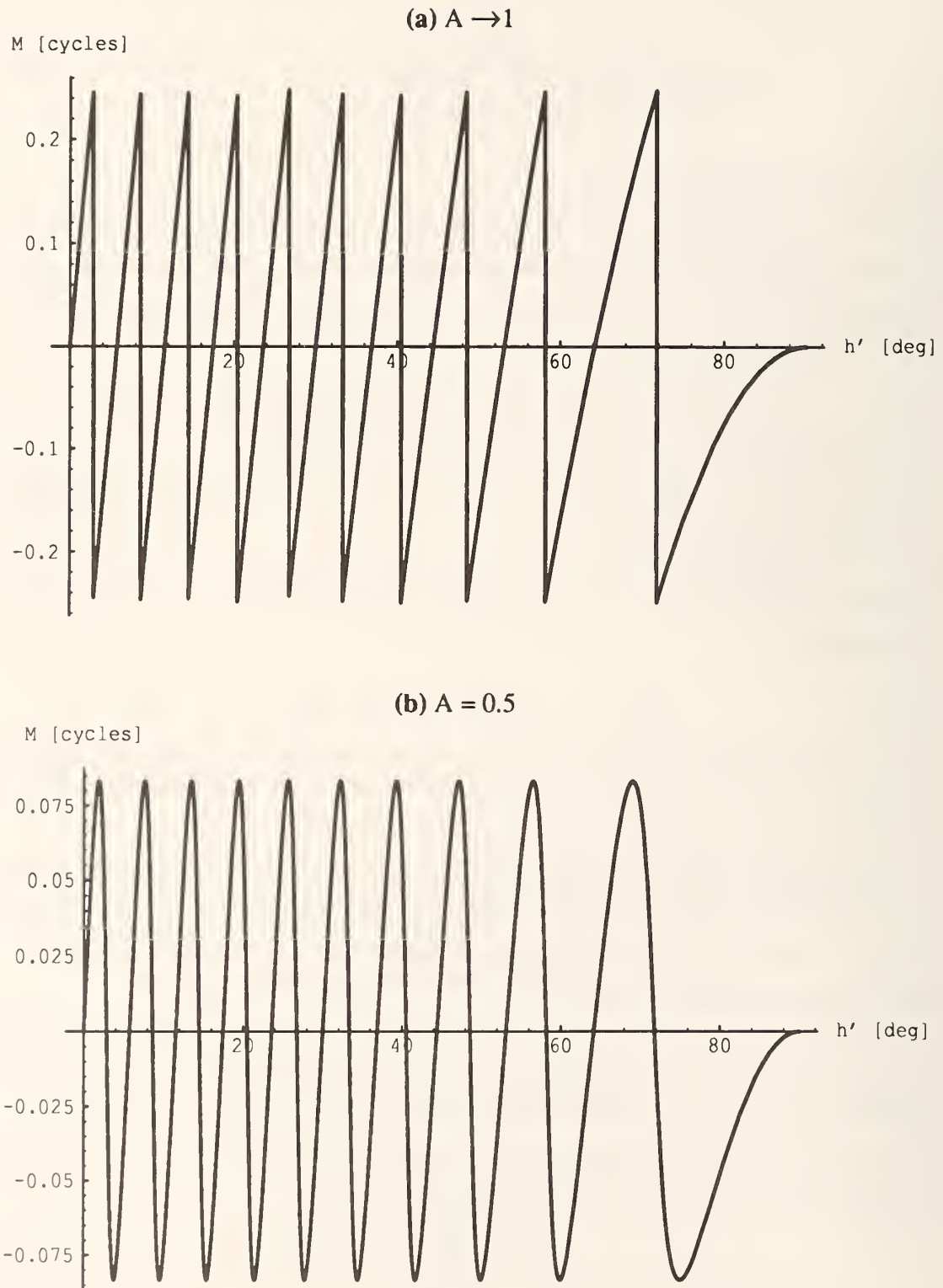


Figure 2.2. Multipath error phase M versus satellite angle above the reflector plane h' for relative multipath amplitudes (a) $A \rightarrow 1$ and (b) $A = 0.5$. In both cases the perpendicular distance from receiver to reflector $d = 1$ m and the wavelength $\lambda = 20$ cm.

2.2 Position Bias Resulting from Phase Error

2.2.1 The Least Squares Adjustment

To be able to calculate how an error in the phase affects the GPS position result, we must understand how GPS infers position from the observed phase. The following discussion of the least squares adjustment is a simplified version of the one given by Rocken [9]. A rigorous general treatment of least squares solutions can be found for example in Vanicek and Krakiwsky [13]. We will use the following variables which each correspond to an observation:

- s : is the true vector from the receiver to a satellite.
- s_o : is the vector from an a priori receiver position to the satellite.
- $\phi(s)$: in cycles is the modeled phase expected at the receiver due to the true receiver and satellite positions.
- ϕ' : in cycles is the actual observed phase which is different from the modelled phase because of unmodelled effects.
- $v = \phi - \phi'$: is called the residual.
- $r = s - s_o$: is a small correction to the a priori receiver position to be found in the adjustment; it is constant for all observations.

We assume here that the only unknowns to be estimated in the adjustment are the three components of the receiver position correction. This is actually the case in practice if the phase ambiguities have been fixed to integer values, precise orbits are used, and no other parameters (e.g., tropospheric delay) are estimated. For each observation there is a set of known model parameters; in the simplified treatment given here it consists only of s_o and constants. Our phase model is simply geometrical neglecting all sorts of errors that would in reality have to be modeled:

$$\phi(s) = \frac{s}{\lambda} = \frac{|s_o + r|}{\lambda} . \quad (2.7)$$

To be able to solve for r we have to linearize eq (2.7). For a priori coordinates close enough to the true positions, r is very small and so

$$\phi(s) \approx \frac{s_o}{\lambda} + \frac{\hat{s}_o \cdot r}{\lambda} . \quad (2.8)$$

It is also

$$\phi(s) = \phi' + v \quad (2.9)$$

and thus

$$v = \frac{s_o}{\lambda} + \frac{\hat{s}_o \cdot r}{\lambda} - \phi' \quad (2.10)$$

For n_{obs} observations included in the adjustment there are n_{obs} equations (2.10) and only three unknowns. The number of observations, e.g., for a daily session in the “EDM” campaign, is on the order of 5000, leading to a highly overdetermined system of equations. In a least squares solution we solve for a correction to the a priori coordinates by requiring the sum of the squares of the residuals to be minimized. Omitting in the following the observation indices present for all variables except r , this requirement is written as

$$\sum_{obs} v^2 = \sum_{obs} \left(\frac{s_o}{\lambda} + \frac{\hat{s}_o \cdot r}{\lambda} - \phi' \right)^2 = \text{minimum}, \quad (2.11)$$

where the sum runs over all observations included in the adjustment.

The minimum is found by differentiation:

$$\frac{\partial}{\partial r} \left(\sum_{obs} v^2 \right) = \sum_{obs} \frac{\partial}{\partial r} \left(\frac{s_o}{\lambda} + \frac{\hat{s}_o \cdot r}{\lambda} - \phi' \right)^2 = 0 \quad (2.12)$$

$$\text{or} \quad \sum_{obs} \left(\frac{s_o}{\lambda} + \frac{\hat{s}_o \cdot r}{\lambda} - \phi' \right) \cdot \hat{s}_o = 0. \quad (2.13)$$

The term $(\hat{s}_o \cdot r) \cdot \hat{s}_o$ can be expressed as $S_o \cdot r$ where S_o is the 3x3 matrix

$$S_{o_{ij}} = \hat{s}_{o_i} \hat{s}_{o_j}. \quad (2.14)$$

Summarizing all the known terms in

$$b \equiv \left(\frac{s_o}{\lambda} - \phi' \right) \cdot \hat{s}_o \quad (2.15)$$

we arrive at

$$\left(\sum_{obs} S_o \right) \cdot \frac{r}{\lambda} = \sum_{obs} b. \quad (2.16)$$

$\left(\sum_{obs} S_o \right)$ is a regular 3x3 matrix and we can finally solve for r :

$$\mathbf{r} = \lambda \cdot \left(\sum_{\text{obs}} \mathbf{S}_o \right)^{-1} \cdot \sum_{\text{obs}} \mathbf{b} . \quad (2.17)$$

Let us now examine the effect of an unmodelled error like multipath on \mathbf{r} . The only term affected by the error is the observations. In our case, we simply have to add the error phase resulting in biased observations $\tilde{\phi} = \phi' + \mathbf{M}$, where $\mathbf{M} = \frac{\mathbf{M}}{2\pi}$ denotes the multipath error phase in cycles. The biased position correction is then

$$\tilde{\mathbf{r}} \equiv \mathbf{r} + \delta\mathbf{r} = \lambda \cdot \left(\sum_{\text{obs}} \mathbf{S}_o \right)^{-1} \cdot \sum_{\text{obs}} (\mathbf{b} - \mathbf{M}\hat{\mathbf{s}}_o) = \mathbf{r} - \lambda \cdot \left(\sum_{\text{obs}} \mathbf{S}_o \right)^{-1} \cdot \sum_{\text{obs}} \mathbf{M}\hat{\mathbf{s}}_o . \quad (2.18)$$

We have thus deduced a general expression for the position bias due to multipath:

$$\delta\mathbf{r} = -\lambda \cdot \left(\sum_{\text{obs}} \mathbf{S}_o \right)^{-1} \cdot \sum_{\text{obs}} \mathbf{M}\hat{\mathbf{s}}_o \quad (2.19)$$

where \mathbf{M} is given by eq (2.6).

2.2.2 Parameterization for Analytical Treatment

We now face the task of actually calculating $\delta\mathbf{r}$ for a given receiver-reflector geometry. All terms of eq (2.19) have been parameterized except the summation over all observations. The direct approach would be to actually perform the summation for a specific GPS session. The matrix \mathbf{S}_o is determined by the known satellite position for each observation; likewise \mathbf{M} can be calculated from the satellite position for each observation. This approach would amount to a GPS simulation experiment in which many error sources are neglected.

We are interested here in a generic solution that may not yield details applicable to a specific practical situation but give some insight to the nature of multipath bias and an order of magnitude estimate of its size. The approach taken is based on the assumption of a uniform satellite distribution throughout the observation session. This assumption is frequently made for the deduction of simple formulae for GPS errors and has been shown to yield results agreeing to within 50 percent with simulation experiments, even for the incomplete satellite test configuration of GPS prior to 1987 [10]. The validity of the assumption will be further discussed in Chapter 4.

The assumption of uniform satellite distribution has to be further defined here: We assume that the satellite positions at the times of observations are evenly distributed in the observation region, defined as angular space covered by the satellites as seen from the receiver in question. In mathematical language this means that the vectors $\hat{\mathbf{s}} \equiv \hat{\mathbf{s}}_o$

belonging to the observations, expressed in spherical coordinates h (elevation angle) and a (azimuth angle) for any coordinate system centered on receiver R (or R'), are distributed in (h, a) -space with a constant density function c .

For a sufficiently high density c we can then parametrize the sum over all observations of any function f depending on \hat{s} as integral over the observation region:

$$\sum_{\text{obs}} f(\hat{s}(h, a)) \rightarrow c \int_{\text{obs}} f(\hat{s}(h, a)) \cosh \cdot dh \cdot da. \quad (2.20)$$

Consequently, eq (2.19) becomes:

$$\delta r = -\lambda \cdot \left(\int_{\text{obs}} S_o \cosh \cdot dh \cdot da \right)^{-1} \cdot \int_{\text{multi}} M \hat{s}_o \cosh \cdot dh \cdot da \quad (2.21)$$

where “multi” denotes the multipath region, i.e., the part of the observation region for which M is nonvanishing.

Let us next calculate the 3×3 matrix

$$\int_{\text{obs}} S_o \cosh \cdot dh \cdot da \equiv B^{-1}.$$

Since the observation region is a cone about the vertical axis, we choose the z -axis of our coordinate system to be vertical and obtain (replacing \hat{s}_o by \hat{s} for convenience):

$$B_{ij}^{-1} = \int_0^{2\pi} \int_{h_{\min}}^{90^\circ} \hat{s}_i \hat{s}_j \cdot \cosh \cdot dh \cdot da \quad (2.22)$$

where h_{\min} is the minimum satellite elevation angle allowed in the adjustment and we assume that there are no obstructing objects within the observation region.

With

$$\hat{s} = \begin{bmatrix} \cosh \cdot \cos a \\ \cosh \cdot \sin a \\ \sinh \end{bmatrix} \quad (2.23)$$

the azimuthal integral vanishes when its integrand is $\cos a$, $\sin a$, and $\cos a \sin a$. Hence, the only non-zero components are:

$$B_{11}^{-1} = \int_{h_{\min}}^{90^\circ} \cos^3 h dh \cdot \int_0^{2\pi} \cos^2 a da \quad (2.24)$$

$$\mathbf{B}_{22}^{-1} = \int_{h_{\min}}^{90^\circ} \cos^3 h dh \cdot \int_0^{2\pi} \sin^2 a da \quad (2.25)$$

$$\mathbf{B}_{33}^{-1} = \int_{h_{\min}}^{90^\circ} \sin^2 h \cosh h dh \cdot \int_0^{2\pi} da. \quad (2.26)$$

All three components are positive with a maximum value of $2/3\pi$ at $h_{\min} = 0$. For a typical elevation cutoff of $h_{\min} = 20^\circ$, \mathbf{B}^{-1} becomes the diagonal matrix

$$\mathbf{B}^{-1} = \begin{bmatrix} 1.06 & 0 & 0 \\ 0 & 1.06 & 0 \\ 0 & 0 & 2.01 \end{bmatrix}. \quad (2.27)$$

Inverting \mathbf{B}^{-1} and inserting the result, \mathbf{B} , into eq (2.21) yields the following analytical formula for the position bias:

$$\delta \mathbf{r} = \begin{bmatrix} \delta x \\ \delta y \\ \delta z \end{bmatrix} = -\lambda \cdot \begin{bmatrix} 1 & 0 & 0 \\ 0 & 1 & 0 \\ 0 & 0 & 0.5 \end{bmatrix} \cdot \int_{\text{multi}} \mathbf{M} \hat{\mathbf{s}}_0 \cosh \cdot dh \cdot da. \quad (2.28)$$

2.3 Generic Calculation for Azimuthal Symmetry

While we succeeded in finding a compact analytical expression for the position bias in terms of receiver-reflector geometry, we are now confronted with the problem that the integral in eq (2.28) is in general very difficult to calculate. The goal of this section is thus to develop a method to simplify eq (2.28) without restricting the applicability of the approach.

2.3.1 Reducing to the Case of Azimuthal Symmetry

In order to obtain eq (2.28) we already chose a coordinate system with vertical z-axis. In this coordinate system \mathbf{M} from eq (2.6) becomes

$$M(h, a) = \text{atan} \left[\frac{\sin \left(\frac{4\pi d}{\lambda} \mathbf{n} \cdot \begin{bmatrix} \cosh \cdot \cos a \\ \cosh \cdot \sin a \\ \sinh \end{bmatrix} \right)}{A^{-1} + \cos \left(\frac{4\pi d}{\lambda} \mathbf{n} \cdot \begin{bmatrix} \cosh \cdot \cos a \\ \cosh \cdot \sin a \\ \sinh \end{bmatrix} \right)} \right] \quad (2.29)$$

and is thus generally dependent on both satellite elevation angle and azimuth in a complicated way. We are still free to rotate the coordinate system about the z-axis and can achieve $n_y = 0$ by choosing the y-axis to be parallel to the reflector surface. Figure 2.3 shows phase contours of M in (h, a) -space for the case of a reflector surface tilted from the horizontal plane by 45° . Numerical integration of the two-dimensional integral in eq (2.28) can be very time consuming (depending on the size of the integration region).

If \mathbf{n} is in z-direction, i.e., the reflector parallel to the horizontal plane, M becomes independent of azimuth. We can reduce the problem to the case of azimuthal symmetry by evaluating the integral in eq (2.28) in a coordinate system in which the z-axis is in direction of \mathbf{n} , i.e., by defining the horizontal plane as parallel to the reflector surface. In this primed coordinate system it is

$$\mathbf{n} = \mathbf{z}' = \begin{bmatrix} 0 \\ 0 \\ 1 \end{bmatrix} \quad \text{and} \quad \hat{\mathbf{s}} = \begin{bmatrix} \cosh' \cdot \cos a' \\ \cosh' \cdot \sin a' \\ \sinh' \end{bmatrix},$$

and thus eq (2.28) becomes

$$M(h') = \text{atan} \left[\frac{\sin \left(\frac{4\pi d}{\lambda} \sinh' \right)}{A^{-1} + \cos \left(\frac{4\pi d}{\lambda} \sinh' \right)} \right]. \quad (2.30)$$

The dependence of M on h' , the satellite elevation above the reflector plane, has already been shown in figure 2.2. With this step we succeeded in separating the dependencies on azimuth and elevation angle in the integral of eq (2.28), which is now

$$m' = \int_{\text{multi}} M(h') \begin{bmatrix} \cosh' \cdot \cos a' \\ \cosh' \cdot \sin a' \\ \sinh' \end{bmatrix} \cosh' \cdot dh' \cdot da'. \quad (2.31)$$

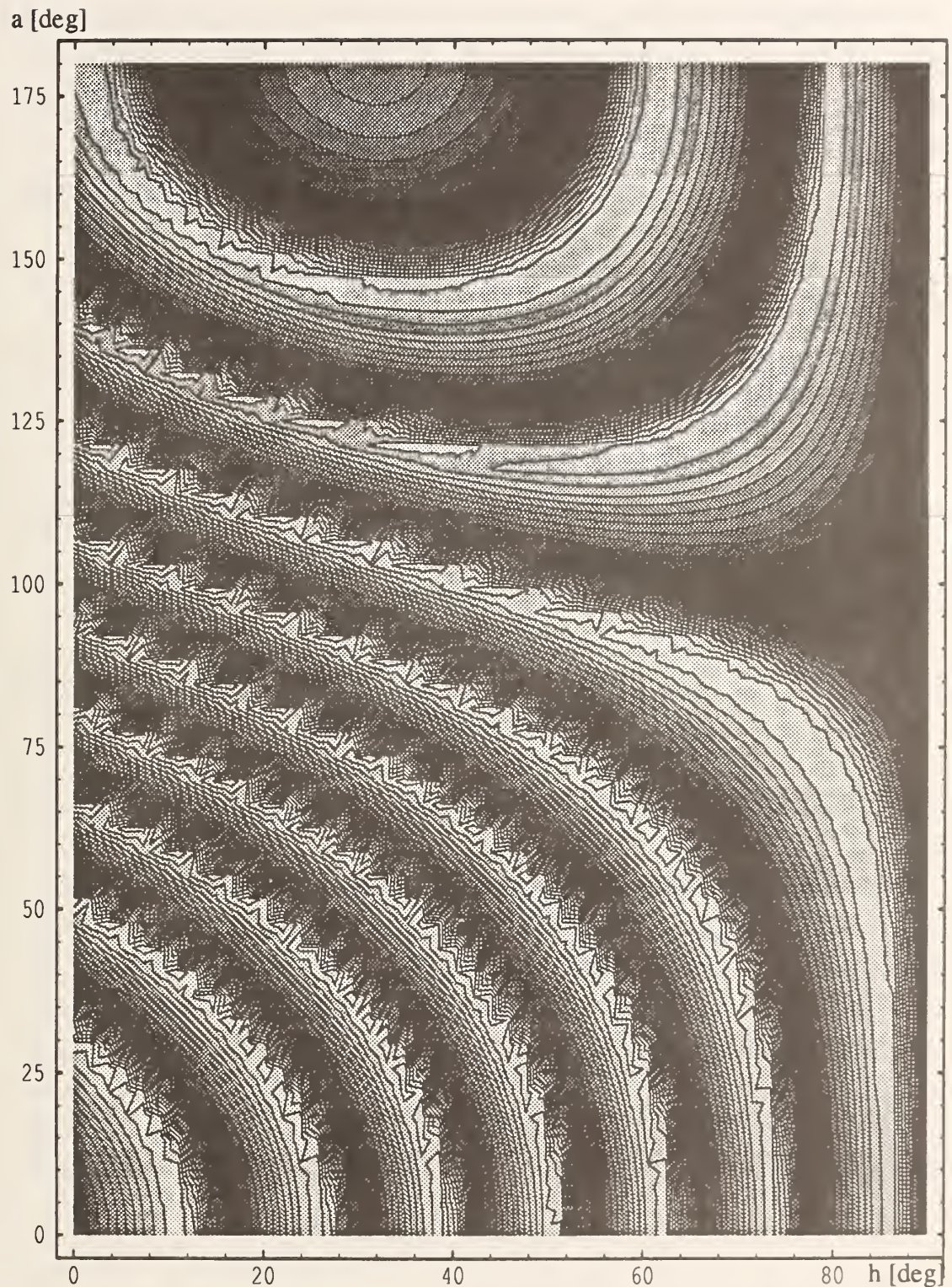


Figure 2.3. Multipath error phase contours as function of satellite elevation h above the horizon and satellite azimuth a as seen from the receiver for a reflector surface tilted 45° with respect to the horizon. Y-axis ($a = 90^\circ$) is parallel to reflector surface. Perpendicular distance to reflector is $d = 0.5$ m, relative multipath amplitude $A = 0.5$, and wavelength $\lambda = 20$ cm. Ragged features are an artifact of the plotting routine.

The components of \mathbf{m}' are given as x,y,z components in the primed coordinate system. As eq (2.28) is given in coordinates of the unprimed system, \mathbf{m}' has to be multiplied by the appropriate rotation matrix \mathbf{T} that transforms from the primed to the unprimed system. The position bias as defined in eq (2.28) is then

$$\delta\mathbf{r} = -\lambda \cdot \mathbf{B} \cdot \mathbf{T} \cdot \mathbf{m}'. \quad (2.32)$$

2.3.2 Numerical Integration

The major task in evaluating eq (2.31) now will be to calculate the following integrals that are part of the components of \mathbf{m}' :

$$\text{in } m_x' \text{ and } m_y': \quad I_{xy} \equiv \int_{h_{\min}}^{h_{\max}} \text{atan} \left[\frac{\sin \left(\frac{4\pi d}{\lambda} \sinh' \right)}{A^{-1} + \cos \left(\frac{4\pi d}{\lambda} \sinh' \right)} \right] \cos^2 h' dh' \quad (2.33)$$

$$\text{and in } m_z': \quad I_z \equiv \int_{h_{\min}}^{h_{\max}} \text{atan} \left[\frac{\sin \left(\frac{4\pi d}{\lambda} \sinh' \right)}{A^{-1} + \cos \left(\frac{4\pi d}{\lambda} \sinh' \right)} \right] \cosh' \sinh' dh', \quad (2.34)$$

where h_{\min} and h_{\max} are limits of the multipath region and have no geometrical meaning at this point.

We first integrate both integrals numerically using the “mathematica” software. The results are shown in figure 2.4 in form of plots of I_{0xy} and I_{0z} as functions of h_{\max} , where the index “0” denotes that $h_{\min} = 0$ (thus $I(h_{\min}, h_{\max}) = I_0(h_{\max}) - I_0(h_{\min})$). Not surprisingly, the integrals $I_0(h_{\max})$ oscillate with the same periodicity as $M(h')$ (compare with figure 2.2). From eq (2.30) one infers that M performs $2d/\lambda$ cycles as h' goes from 0 to 90° (and \sinh' from 0 to 1). Hence, the average oscillation period in h' -space is $\lambda/(2d) \cdot 90^\circ$; for $d = 1$ m it is approximately 9° . From now on, all terms concerning oscillation parameters (period, frequency, cycle, etc.) shall refer to the oscillations in h' .

2.3.3 Approximating the Elevation Integrals

Given the apparent sinusoidal features of M and the integrals I_{0xy} and I_{0z} , it is tempting to simply approximate them by harmonic functions of appropriate amplitude

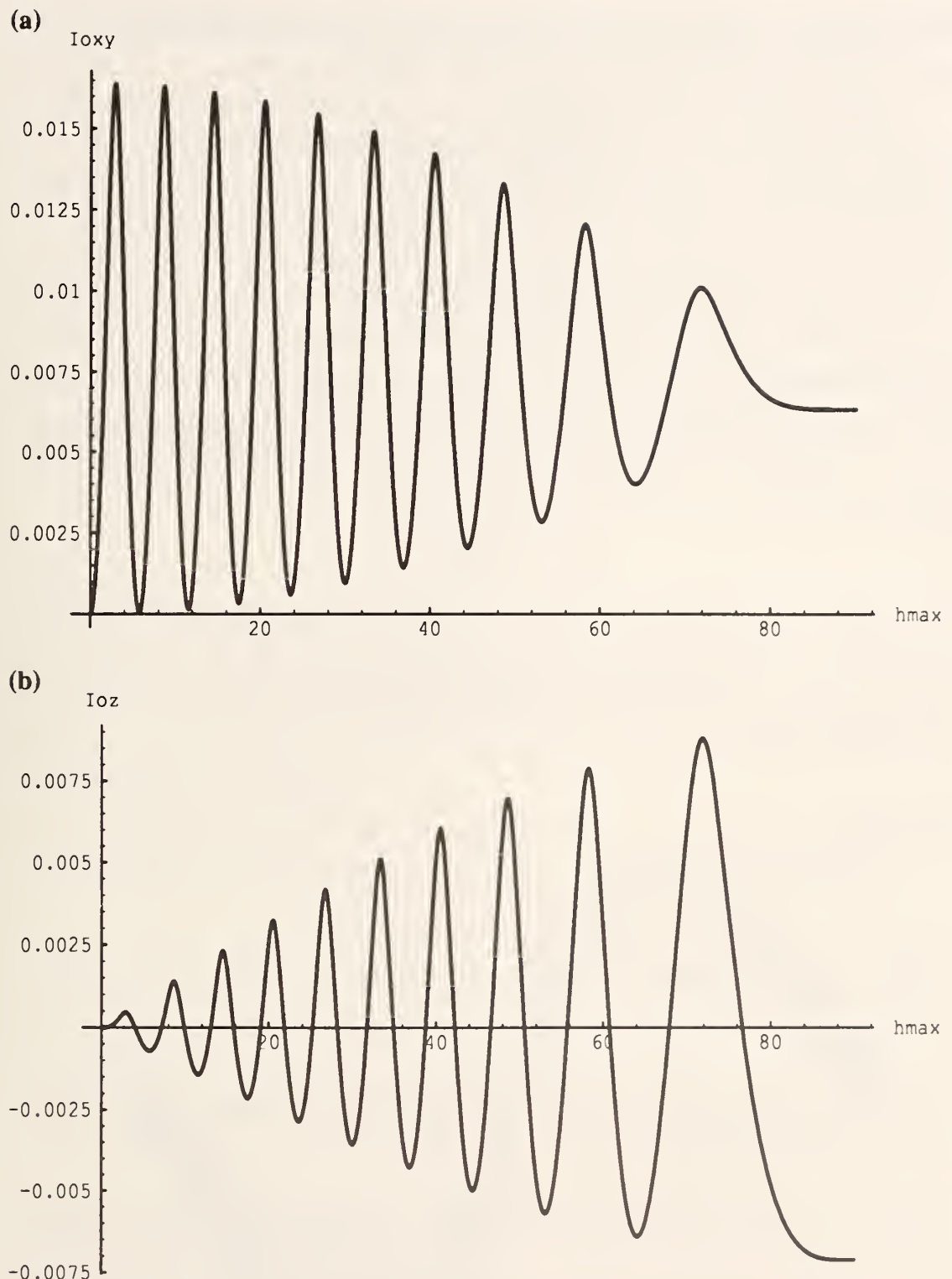


Figure 2.4. Numerical integration of the integrals (a) $I_{0xy} = I_{xy}(h_{\min}=0)$ and (b) $I_{0z} = I_{xy}(h_{\min}=0)$ as functions of upper integration limit h_{\max} . Relative multipath amplitude is $A = 0.5$, perpendicular distance to reflector $d = 1$ m, and wavelength $\lambda = 20$ cm.

and frequency to facilitate analytic expressions for the integrals. We will now investigate how far such approximations would yield meaningful results.

$M(h')$ is different from a sine function in two ways: Its shape within one period is not quite harmonic and its frequency in h' -space varies with h' . The latter is due to the \sinh 's in eq (2.30). Let us look at the shape first and examine instead of $M(h')$ the function

$$M(x) \equiv \text{atan} \left[\frac{\sin x}{A^{-1} + \cos x} \right], \quad (2.35)$$

whose periodicity in x is, of course, constant. It is easily seen that for $A \rightarrow 0$, $M(x) \rightarrow A \sin x$. For larger A we may still attempt to apply this approximation; however, the amplitude of the oscillation may be notably different from A . It can be shown that the maximum value of M for a given A is simply

$$M_{\max} = a \sin A. \quad (2.36)$$

The shape of $M(x)$ is shown in figure 2.5 for different A 's together with the approximation, $M_{\max} \sin x$. In practice, A is likely to be small. At any rate, the exact shape of M has no influence on the maximum amplitude of integrals I_{xy} and I_z which will be our main concern here.

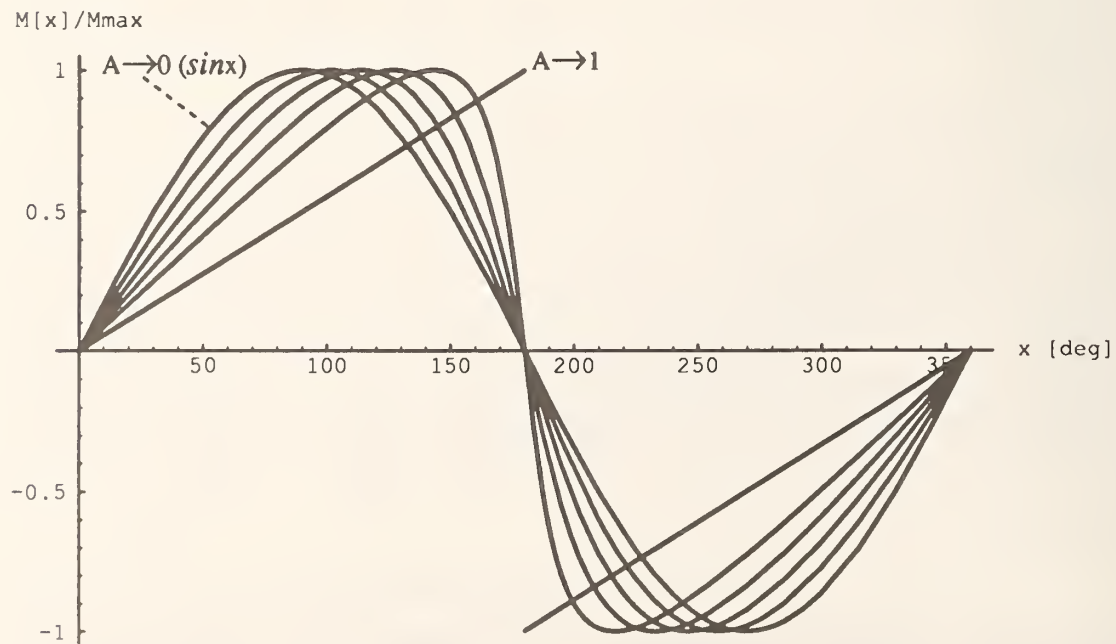


Figure 2.5. $M(x)$ normalized to amplitude 1 for varying A 's: Plots are progressing from $A \rightarrow 0$ (= the approximation $\sin x$) over $A = 0.2, 0.4, 0.6, 0.8$ to $A \rightarrow 1$.

Having approximated $M(x)$ with $M_{\max} \sin x$, we now return to $M(h')$ which has become

$$\tilde{M}(h') \equiv M_{\max} \cdot \sin\left(\frac{4\pi d}{\lambda} \sinh h'\right). \quad (2.37)$$

Unfortunately, there is still no simple analytic expression for the integrals if eq (2.37) is used instead of $M(h')$. To gain some insight into the factors determining the shape of the integrals I_{0xy} and I_{0z} we further simplify this expression by replacing the inside sine with a linear function that yields the same number of cycles of M in a satellite pass. In other words, we approximate $\tilde{M}(h')$ by a sine function with a constant frequency equal to the average frequency of $M(h')$. As already deduced above, the average period is $\frac{\lambda}{2d} \cdot \frac{\pi}{2}$ and thus the average angular frequency is

$$\Omega \equiv \frac{8d}{\lambda}. \quad (2.38)$$

This results in

$$\bar{M}(h') = M_{\max} \sin \Omega h' = a \sin A \cdot \sin\left(\frac{8d}{\lambda} h'\right). \quad (2.39)$$

Note that with this step we just replaced $\sinh h'$ by $\frac{2}{\pi} \cdot h'$, its average slope in the interval $[0, \pi/2]$ to which h' is confined.

The integrals containing $\bar{M}(h')$ instead of $M(h')$ can easily be evaluated. The solutions in the limit $\Omega \gg 1$ are:

$$\overline{I_{0xy}} \equiv \int_0^{h_{\max}} M_{\max} \sin \Omega h' \cdot (\cosh h')^2 dh' \rightarrow \frac{M_{\max}}{\Omega} [1 - \cos \Omega h_{\max} \cos^2 h_{\max}] \quad (2.40)$$

$$\overline{I_{0z}} \equiv \int_0^{h_{\max}} M_{\max} \sin \Omega h' \cdot \cosh' \sinh' dh' \rightarrow -\frac{M_{\max}}{\Omega} \cdot \frac{1}{2} \cos \Omega h_{\max} \sin 2h_{\max}. \quad (2.41)$$

General features of the integrals apparent from eqs (2.40) and (2.41) are:

- They oscillate with frequency Ω .
- Their maximum amplitude is proportional to M_{\max}/Ω .
- The oscillation amplitudes vary as $\cos^2 h_{\max}$ and $\sin 2h_{\max}$ for $\overline{I_{0xy}}$ and $\overline{I_{0z}}$, respectively.

Comparing these integrals with the exact integrals of figure 2.4 we find:

- Using the values of $A = 0.5$, $d = 1 \text{ m}$, and $\lambda = 20 \text{ cm}$, the maximum amplitudes of $\overline{I_{0xy}}$ and $\overline{I_{0z}}$ are 0.013 and 0.0065. Thus, the approximation somewhat overestimates the maximum value for I_{0xy} and underestimates it for I_{0z} . This is due to the fact that the region of faster-than-average oscillations (small h') is weighted by $\cos^2 h' \approx 1$ in I_{0xy} , i.e., relatively overweighted, but by $\sinh' \cosh' \approx h'$ in I_{0z} , i.e., relatively underweighted.
- There are significant deviations in the shapes of the oscillation envelopes, particularly obvious in I_{0z} . This integral differs much more strongly because the region near $h' = 90^\circ$, which deviates most strongly from the average frequency (oscillation frequency $\rightarrow 0$), receives the most weight.

We now argue that these general results, and especially the envelope shapes of the exact integrals, are not dependent on the particular values of A and d/λ :

- A will only influence the shape of the oscillation and determine the scale of the vertical axis proportional to $M_{\max} = a \sin A$.
- $d/\lambda \propto \Omega$ is proportional to the number of cycles on the horizontal axis. Integrals of oscillating functions scale with the inverse frequency of the integrand. Thus, the vertical scale of the exact integrals will be proportional to λ/d .

We may thus construct approximations to I_{0xy} and I_{0z} by simulating the features as apparent in figure 2.4. Starting from eqs (2.40) and (2.41) we make the following “corrections”:

- (1) Scale the amplitudes to the correct values of I_{0xy} and I_{0z} . These are found numerically to be both approximately 0.016 for the values $A = 0.5$, $d = 1 \text{ m}$, and $\lambda = 20 \text{ cm}$ used in figure 2.4.
- (2) Observe from figure 2.4. that the envelope shapes of the exact integrals are very close to \cosh_{\max} and \sinh_{\max} , respectively.
- (3) Include the frequency dependence; as the integrals display the same frequency dependence as their integrand $M(h')$, we can simply replace Ωh by the original argument, $\frac{4\pi d}{\lambda} \sinh$.

We thus arrive at our final (empirical) approximations to I_{0xy} and I_{0z} :

$$\tilde{I}_{0xy} \equiv 0.62 \cdot \frac{M_{\max} \lambda}{8d} \left[1 - \cosh_{\max} \cos \left(\frac{4\pi d}{\lambda} \sinh_{\max} \right) \right] \quad (2.42)$$

$$\tilde{I}_{0z} \equiv -0.61 \cdot \frac{M_{\max} \lambda}{8d} \sinh_{\max} \cos \left(\frac{4\pi d}{\lambda} \sinh_{\max} \right). \quad (2.43)$$

Plots of these approximations together with the exact integrals are shown in figure 2.6. The agreement is quite surprising; one might presume that the empirically constructed approximations could be obtained through more rigorous mathematical reasoning as well. We will not follow that path but accept that the lack of mathematical scrutiny requires us to be critical of the approximations. Clearly, their quality will decline for small d (we assumed $\Omega \gg 1$ in eqs (2.40) and (2.41)). The real bias in the limit $d = 0$ obviously has to vanish, while according to eqs (2.42) and (2.43) it becomes infinite. Intuitively, it is clear that these expressions will only be meaningful as long as the integrals perform at least one full cycle between 0 and 90° . This is the case for $2d/\lambda = 1$, i.e., $d = \lambda/2$. In particular, the integrals will start to grow slower than $\propto 1/d$ when d is on the order of or smaller than one wavelength; finally they vanish for very small d . We will take the approximations as valid in that they give a good estimate for the amplitude and frequency of the oscillations for a given h_{\max} and d bigger than 1 m (the value chosen in figure 2.6); for smaller d they overestimate the amplitudes. This will be sufficient for our purpose.

Summarizing, we state that the elevation integrals I_{0xy} and I_{0z} oscillate in h_{\max} with an average period of $2\pi/\Omega = 45^\circ\lambda/d$ under (approximately) cosine and sine envelopes, respectively. The maximum amplitude reached is about $0.077 M_{\max}\lambda/d$ for both integrals. I_{0xy} is always positive while I_{0z} oscillates about zero.

2.4 Generalization to Dual Frequency Observations

The treatment so far has been restricted to a single frequency while most experiments today (and the “EDM” experiment) use dual frequency observations of the L1 and L2 carriers to correct for the ionospheric delay. It is clear that the ionosphere free linear combination L3 will be contaminated by multipath from both L1 and L2 and thus be noisier than the single frequency signals. This now has to be quantified.

The ionosphere corrected phase in cycles of L1 is defined as (e.g., [9])

$$\phi_3 \equiv \phi_1 - C \cdot \left(\phi_1 - \frac{\omega_1}{\omega_2} \phi_2 \right) = 2.545\phi_1 - 1.984\phi_2 \quad (2.44)$$

where ϕ_1 and ϕ_2 are both in cycles of their respective wavelengths and

$$C \equiv \frac{\omega_2^2}{\omega_2^2 - \omega_1^2} = -1.545. \quad (2.45)$$

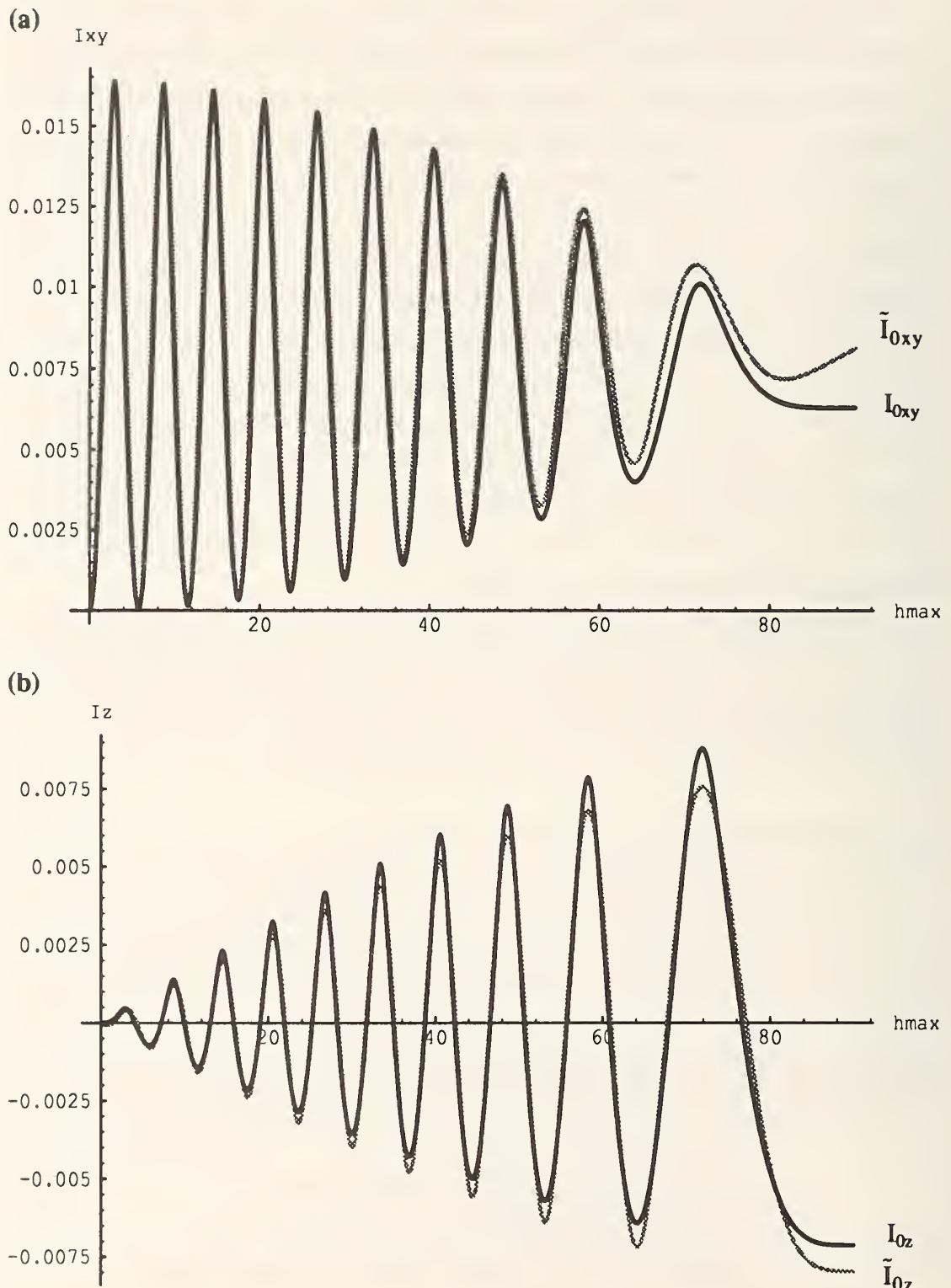


Figure 2.6. Exact integrals (black lines) and approximated integrals (gray lines): (a) I_{0xy} and \tilde{I}_{0xy} , (b) I_{0z} and \tilde{I}_{0z} as functions of their upper integration limit h_{\max} . Relative multipath amplitude is $A = 0.5$, perpendicular distance to reflector $d = 1$ m, and wavelength $\lambda = 20$ cm.

It follows that the multipath error phase in L3 is

$$M_3 = 2.545M_1 - 1.984M_2, \quad (2.46)$$

M_1 and M_2 being defined by eq (2.6) with λ equal to λ_1 and λ_2 , respectively. Assuming equal relative amplitudes $A_1 = A_2 = A$ of the reflected signals of L1 and L2 and using approximation eq (2.37) this becomes

$$\tilde{M}_3(h') = M_{\max} \left[2.545 \sin\left(\frac{4\pi d}{\lambda_1} \sinh'\right) - 1.984 \sin\left(\frac{4\pi d}{\lambda_2} \sinh'\right) \right]. \quad (2.47)$$

Let

$$\psi_i \equiv \frac{4\pi d}{\lambda_i} \sinh', \quad \Delta\psi \equiv \psi_1 - \psi_2, \quad C_1 \equiv 2.545, \quad C_2 \equiv 1.984,$$

then eq (2.47) can be expressed as

$$\tilde{M}_3 = D \sin \left[\operatorname{atan} \left(\frac{C_1 \sin \psi_1 + C_2 \sin \psi_2}{C_1 \cos \psi_1 + C_2 \cos \psi_2} \right) \right] \quad (2.48)$$

where $D = M_{\max} \sqrt{C_1^2 + C_2^2 - 2C_1C_2 \cos \Delta\psi}.$ (2.49)

This means that the maximum amplitude of M_3 is

$$D_{\max} = M_{\max} (C_1 + C_2) = a \sin A \cdot 4.529 \quad (2.50)$$

as long as $\Delta\psi$ reaches the value π . For a satellite that passes $h' = 90^\circ$ this is the case if $4\pi d(1/\lambda_1 - 1/\lambda_2) > \pi$, i.e., $d > 23$ cm which is usually satisfied in practice. In other words, the multipath noise of the L3 linear combination is in general about 4.5 times as large as for the single frequencies unless the receiver is mounted very close to the ground and no other reflectors are present.

We have to examine now how this translates into the position bias. If L3 is used as observable, then the simple phase model eq (2.7) becomes

$$\phi_3(s) = \frac{s}{\lambda_1}. \quad (2.51)$$

It follows that the corresponding formula for the position bias is obtained by simply replacing M with M_3 and λ with λ_1 in eq (2.28):

$$\delta r = -\lambda_1 \cdot B \cdot \int_{\text{multi}} M_3 \hat{s}_o \cosh \cdot dh \cdot da. \quad (2.52)$$

Hence, the problem only amounts to calculating differences of integrals that have been solved already. Any integral I_3 involving M_3 in the integrand is calculated from the respective integrals I_1 and I_2 with M_1 and M_2 as $I_3 = C_1 I_1 - C_2 I_2$:

$$\begin{aligned} I_{30xy} &\approx \tilde{I}_{30xy} = C_1 \tilde{I}_{10xy} - C_2 \tilde{I}_{20xy} \\ &= 0.62 M_{\max} \left[\frac{C_1}{\Omega_1} (1 - \cosh_{\max} \cos \psi_1) - \frac{\lambda_2 C_2}{\lambda_1 \Omega_1} (1 - \cosh_{\max} \cos \psi_1) \right] \\ &\equiv -0.62 \frac{M_{\max} \lambda_1}{8d} \cosh_{\max} (2.545 \cos \psi_1 - 2.506 \cos \psi_2), \end{aligned} \quad (2.53)$$

$$\begin{aligned} I_{30z} &\approx \tilde{I}_{30z} = C_1 \tilde{I}_{10z} - C_2 \tilde{I}_{2z} \\ &= -0.61 M_{\max} \left(\frac{C_1}{\Omega_1} \sinh_{\max} \cos \psi_1 + \frac{\lambda_2 C_2}{\lambda_1 \Omega_1} \sinh_{\max} \cos \psi_2 \right) \\ &\equiv -0.61 \frac{M_{\max} \lambda_1}{8d} \sinh_{\max} (2.545 \cos \psi_1 - 2.506 \cos \psi_2). \end{aligned} \quad (2.54)$$

Plots of \tilde{I}_{30xy} and \tilde{I}_{30z} are shown in figure 2.7 together with the exact (numerically integrated) integrals I_{30xy} and I_{30z} for the usual parameters of $A = 0.5$ and $d = 1$ m. The envelopes, simply \cosh_{\max} and \sinh_{\max} for single wavelengths, are now modified through the interference of the two wavelengths that is dependent on d . This modification is calculated in the same way as the amplitude of M_3 above in eq (2.49):

$$2.545 \cos \psi_1 - 2.506 \cos \psi_2 = E \cos \Phi, \quad (2.55)$$

where the amplitude

$$\begin{aligned} E &= \sqrt{2.545^2 + 2.506^2 - 2 \cdot 2.545 \cdot 2.506 \cos \Delta \psi} \\ &\approx \sqrt{2 \cdot 2.545 \cdot 2.506} \cdot \sqrt{1 - \cos \Delta \psi} = 5.05 \sin \frac{\Delta \psi}{2} \end{aligned} \quad (2.56)$$

and Φ is the phase of the fast oscillations with an average period on the order of

$$p = \frac{2\pi}{\Omega} = \frac{4\pi}{\Omega_1 + \Omega_2} \equiv \frac{10^\circ}{d [m]}. \quad (2.57)$$

The periodicity of the amplitude variation, on the other hand, is on the order of

$$P = \frac{4\pi}{\Delta \Omega} \equiv \frac{80^\circ}{d [m]}. \quad (2.58)$$

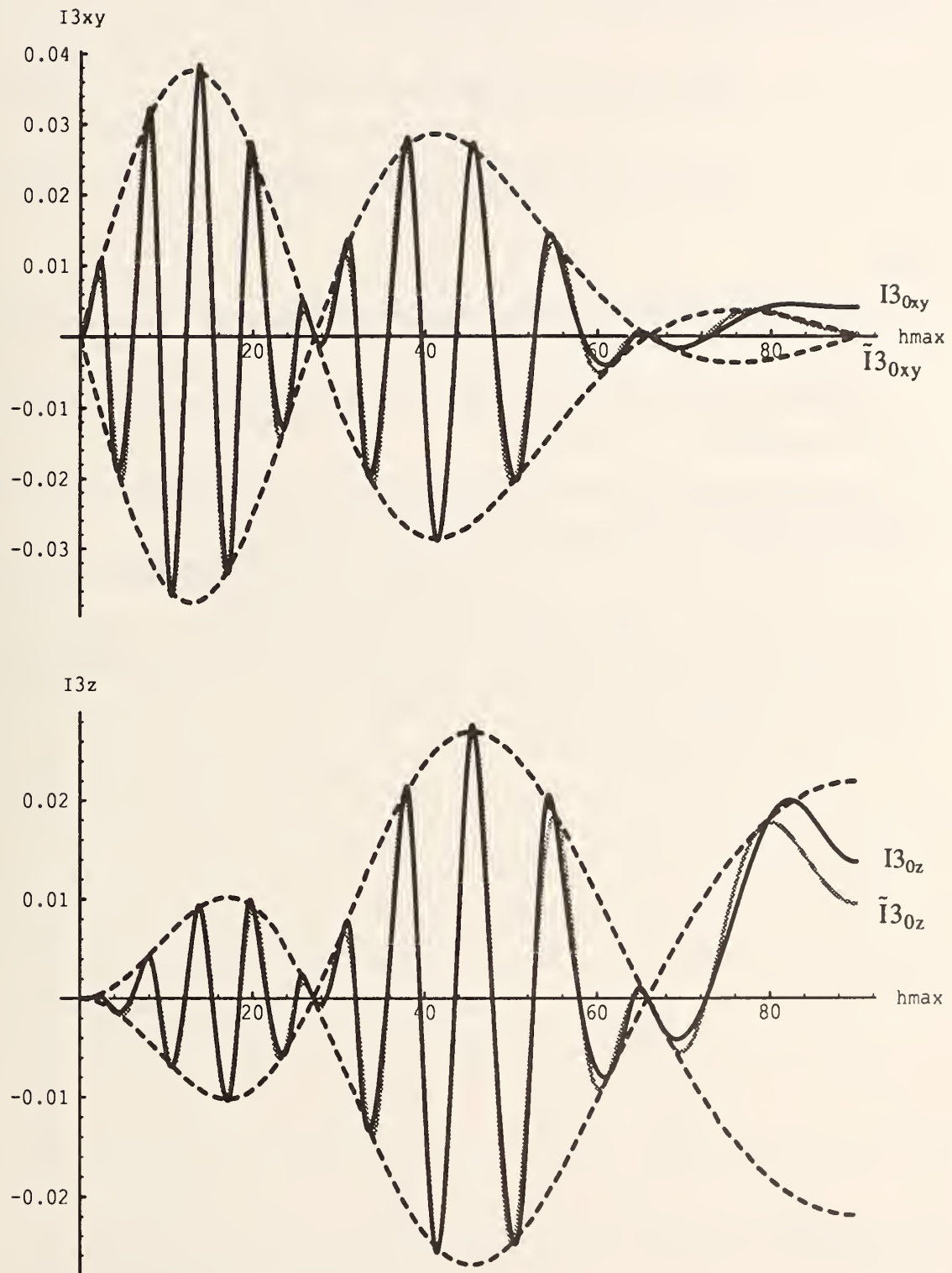


Figure 2.7. Exact integrals (black lines) and approximated integrals (gray lines): (a) $I3_{0xy}$ and $I3_{0xy}$, (b) $I3_{0z}$ and $I3_{0z}$ as functions of their upper integration limit h_{\max} . Dashed lines are the amplitude envelopes calculated from the approximations. Relative multipath amplitude is $A = 0.5$, perpendicular distance to reflector $d = 1$ m, and wavelengths $\lambda_1 = 19$ cm and $\lambda_2 = 24$ cm.

The resulting envelopes, also shown in figure 2.7, are:

$$\tilde{I}3_{0xy}^{\text{env}}(h_{\max}) = 3.1 \frac{M_{\max} \lambda_1}{8d} \cosh_{\max} \sin \frac{\Delta\psi}{2} \quad (2.59)$$

$$\tilde{I}3_{0z}^{\text{env}}(h_{\max}) = 3.1 \frac{M_{\max} \lambda_1}{8d} \sinh_{\max} \sin \frac{\Delta\psi}{2} \quad (2.60)$$

with

$$\frac{\Delta\psi}{2} = 2\pi d \left(\frac{1}{\lambda_1} - \frac{1}{\lambda_2} \right) \sinh_{\max} \approx 6.9 \cdot d [\text{m}] \sinh_{\max}. \quad (2.61)$$

Comparing these results with the ones of the preceding section for single frequency observations ($\lambda = \lambda_1$) we find:

- The elevation integrals $I3_{0xy}$ and $I3_{0z}$ oscillate in h_{\max} with about the same period as the corresponding single-frequency integrals, i.e., $10^\circ/d[\text{m}]$.
- The oscillation envelopes are still cosine and sine functions, respectively, that now undergo sinusoidal variations with an average period of $80^\circ/d[\text{m}]$.
- The maximum amplitude reached is about five times as big as in the single frequency case, namely $3.1 M_{\max} \lambda_1 / 8d = 0.074 M_{\max} / d$.
- Both integrals oscillate about zero.

CHAPTER 3

CALCULATIONS FOR SIMPLE REFLECTOR GEOMETRIES

3.1 Outline of the Strategy

With the tools developed in the previous chapter we are now able to calculate the position bias due to multipath for simple reflector-receiver geometries. The general strategy, whenever applicable, will be:

- (1) Define the reflector geometry in a coordinate system with vertical z-axis (the unprimed system or “u-system”). We will generally define the y-axis parallel to the reflector surface and assume a reflector horizontally symmetrical with respect to the x-axis, which reduces the problem to two dimensions.
- (2) Define a suitable coordinate system centered on the image receiver R' with the z-axis in the direction of the normal vector of the reflector surface (the primed system or “p-system”) to reduce the calculation to the case of azimuthal symmetry.
- (3) Determine the rotation matrix T that transforms from the p- to the u-system.
- (4) Parameterize the multipath region (defined in section 2.2.2) in terms of elevation angle h' and azimuth a' of the p-system.
- (5) The position bias in the u-system is then calculated according to eq (2.32) as

$$\delta \mathbf{r}_{1/3} = \begin{bmatrix} \delta x \\ \delta y \\ \delta z \end{bmatrix} = -\lambda_1 \cdot \mathbf{B} \cdot \mathbf{T} \cdot \int_{\text{multi}} \mathbf{M}_{1/3}(h') \begin{bmatrix} \cosh' \cdot \cos a' \\ \cosh' \cdot \sin a' \\ \sinh' \end{bmatrix} \cosh' \cdot dh' \cdot da' \quad (3.1)$$

where the index “1/3” stands for either single frequency (L1) observations or dual frequency (L3) observations.

- (6) The values of the elevation integrals $I(h_{\min}, h_{\max})$ occurring in eq (3.1) are in principle calculated from the approximations developed in the last chapter as

$$I(h_{\min}, h_{\max}) \equiv \tilde{I}_0(h_{\max}) - \tilde{I}_0(h_{\min}). \quad (3.2)$$

(7) These integrals oscillate in h_{\min} and h_{\max} with frequencies (and in the L3-case also amplitude variations) depending on d as discussed in chapter 2. We are neither interested in the position bias for narrowly defined values of d or $h_{\min/\max}$, nor would it be justified on the basis of the approximations made to attempt such a calculation. Instead, we will generally only estimate an upper limit to the magnitude of an elevation integral as

$$|I(h_{\min}, h_{\max})| \leq \tilde{I}_0^{\max}(h_{\min}) + \tilde{I}_0^{\max}(h_{\max}), \quad (3.3)$$

where $\tilde{I}_0^{\max}(h_{\min}) \geq 0$ and $\tilde{I}_0^{\max}(h_{\max}) \geq 0$ are the oscillation amplitudes of the corresponding I_0 integral for the particular values of h_{\min} and h_{\max} (ignoring the envelope variations in the L3-case). These oscillation amplitudes are

- for single frequency observations (deduced from eqs (2.42) and (2.43)):

$$\tilde{I}_{0xy}^{\max}(h_{\max}) \equiv 0.6 \frac{\lambda_1 M_{\max}}{8d} \cosh h_{\max} \equiv 0.015 \cdot \frac{M_{\max}}{d} \cosh h_{\max} \quad (3.4)$$

$$\tilde{I}_{0z}^{\max}(h_{\max}) \equiv 0.6 \frac{\lambda_1 M_{\max}}{8d} \sinh h_{\max} \equiv 0.015 \cdot \frac{M_{\max}}{d} \sinh h_{\max} \quad (3.5)$$

- for dual frequency observations (deduced from eqs (2.59) to (2.60)):

$$\tilde{I}_{0xy}^{\max}(h_{\max}) \equiv 3 \frac{\lambda_1 M_{\max}}{8d} \cosh h_{\max} \equiv 5 \cdot \tilde{I}_{0xy}^{\max}(h_{\max}) \quad (3.6)$$

$$\tilde{I}_{0z}^{\max}(h_{\max}) \equiv 3 \frac{\lambda_1 M_{\max}}{8d} \sinh h_{\max} \equiv 5 \cdot \tilde{I}_{0z}^{\max}(h_{\max}). \quad (3.7)$$

The sign of the bias cannot be inferred in these estimates because the integrals oscillate about zero (with the only exception of I_{0xy} which is always positive). We keep in mind that the maximum value $\tilde{I}_0^{\max}(h_{\min}) + \tilde{I}_0^{\max}(h_{\max})$ may be reached whenever h_{\max} and h_{\min} are more than a quarter cycle of the oscillations apart, i.e.,

$$\Delta h \equiv h_{\max} - h_{\min} \geq \frac{2^\circ}{d [m]}. \quad (3.8)$$

This may as well be viewed as a condition for d . In the L3 case the integrals do not oscillate at their highest values unless also the first maximum of the amplitude variations is reached (compare figure 2.7) which requires

$$h_{\min} \cdot d [m] \geq 20^\circ. \quad (3.9)$$

Note that the integrals do not grow any further for decreasing d if eqs (3.8) and (3.9) are not satisfied and in fact vanish for very small d . The highest possible values are thus approximately reached for $d \approx 2^\circ/\Delta h$ and $d \approx 20^\circ/h_{\max}$ for the L1- and L3-case, respectively. Remember, however, that the calculations are no longer useful if d becomes comparable to a wavelength, i.e., about 20 cm.

In this chapter M (without underscore) shall be in units of cycles. All definitions and calculations of integrals from the last chapter will remain valid by simply expressing $M_{\max} = \pi/4$ in units of cycles, too. This means that the maximum value M_{\max} can assume is now 1/4. Whenever unitless lengths occur in equations they are understood as numbers in meters.

3.2 Multipath from Flat Ground

3.2.1 Full Azimuthal Symmetry

Consider the ideal receiver site; a perfectly flat ground and no objects anywhere nearby. Even in this case there exists multipath from ground reflections that reach the antenna phase center from the backplane. The geometry is elementary; d is the antenna height above the ground. The normal vector of the reflector plane (the ground) is vertical, thus the u - and p - coordinate systems are identical. Moreover, there are reflections for any satellite position within the observation region; thus the multipath region is identical to the observation region. Consequently, the position bias is calculated as

$$\delta r = \begin{bmatrix} \delta x \\ \delta y \\ \delta z \end{bmatrix} = -\lambda_1 \cdot B \cdot \int_0^{2\pi} \int_{h_{\min}}^{90^\circ} M(h') \begin{bmatrix} \cosh h' \cdot \cos a' \\ \cosh h' \cdot \sin a' \\ \sinh h' \end{bmatrix} \cosh h' \cdot dh' \cdot da' \quad (3.10)$$

where h_{\min} is the minimum satellite elevation included in the adjustment, typically 20° . As expected due to the azimuthal symmetry of the multipath region, there is no horizontal bias; the azimuthal integral vanishes for δx and δy . The vertical bias for single frequency observations is

$$\begin{aligned}
|\delta z_1| &= \lambda_1 \cdot 0.5 \cdot 2\pi \cdot I1_z(20^\circ, 90^\circ) \\
&\leq \lambda_1 \pi [\tilde{I}1_{0z}^{\max}(20^\circ) + \tilde{I}1_{0z}^{\max}(90^\circ)] \\
&= (\lambda_1 \pi) 0.015 \frac{M_{\max}}{d} (\sin 20^\circ + \sin 90^\circ) \approx 12 \text{ mm} \cdot \frac{M_{\max}}{d}. \quad (3.11)
\end{aligned}$$

For dual frequency observations the bias may be five times as large:

$$|\delta z_3| \leq 60 \text{ mm} \cdot \frac{M_{\max}}{d}. \quad (3.12)$$

3.2.2 Disturbed Symmetry

The non-existence of horizontal bias in the preceding section is due to the azimuthal symmetry of the multipath region; the effects of multipath from all sides cancel each other. Consider now the effect if this symmetry is disturbed because multipath in a particular region is eliminated, e.g., by some obstructing object or by decreased ground reflectivity or simply “missing ground” due to a nearby cliff. The geometry is illustrated in figure 3.1.

The vertical bias calculated in the preceding section is not expected to change much due to the region of missing multipath. However, a horizontal bias is now introduced. Instead of integrating over the multipath region we can as well integrate over

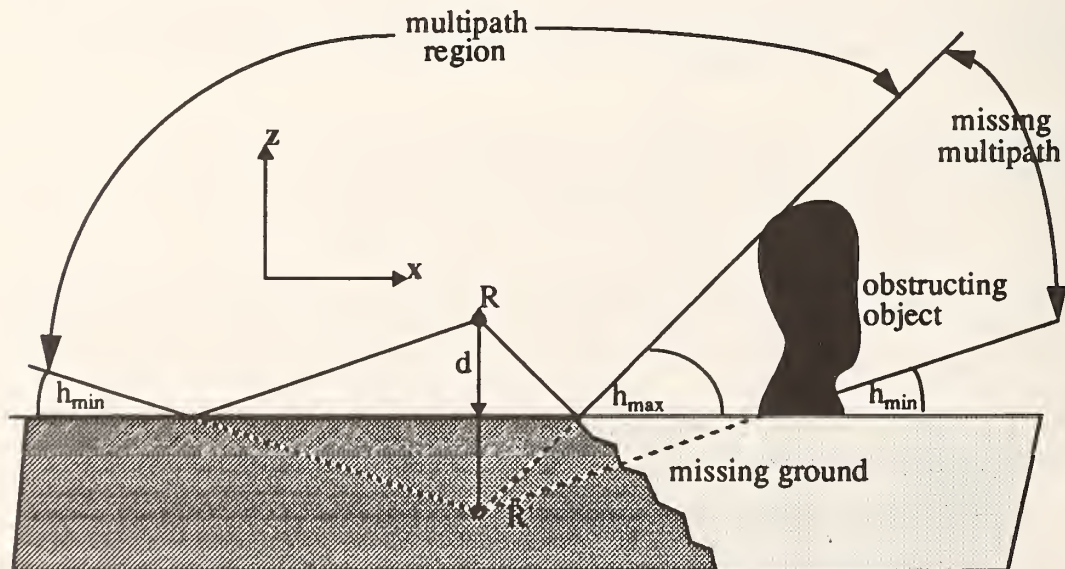


Figure 3.1. Asymmetrical multipath region for flat ground as reflector.

the region of missing multipath knowing that the integral over both together vanishes. Let us assume that this region is horizontally symmetrical with respect to the x-axis, has a maximum angular height h_{\max} at $a = 0$, and a maximum azimuthal extent from $+a_{\max}$ to $-a_{\max}$ ($a_{\max} \leq \pi/2$) as seen from the image receiver R'. While the integration limits of the elevation angle are, in general, functions of azimuth depending on the exact shape of the region of missing multipath, we can obtain an upper limit to the bias by separating the elevation and azimuthal integrals and integrating each over the maximum extent of the region:

$$\left| \int_{\text{multi}} M(h') \cos^2 h' \left(\frac{\cos a}{\sin a} \right) dh da \right| \leq \left| \int_{h_{\min}(a=0)}^{h_{\max}(a=0)} M(h') \cosh' dh \right| \left| \int_{-a_{\max}}^{a_{\max}} \left(\frac{\cos a}{\sin a} \right) da \right|. \quad (3.13)$$

This inequality has to be understood in an upper-limit sense, i.e., the elevation integral on the right hand side really should be thought of as its oscillation amplitude as estimated by the method described in section 3.1. We thus assign the elevation integral its maximum value for its limits at $a = 0$ throughout all the azimuthal integration. In most practical situations the elevation integral will go through several maxima and minima as its limits as functions of azimuth span an interval of several times $2^\circ/d$. When applying these calculations to the practice, it ought to be kept in mind that eq (3.13) may be quite an overestimate.

The choice of symmetry about the x-axis causes the integral over $\sin a$ and thus the bias in the y-direction to vanish. The bias along the x-axis is for L1 observations

$$\begin{aligned} |\delta x_1| &\leq \lambda_1 \cdot 2 \sin a_{\max} \cdot [\tilde{I}_{0xy}^{\max}(h_{\min}) + \tilde{I}_{0xy}^{\max}(h_{\max})] \\ &\approx 6 \text{ mm} \cdot \frac{M_{\max}}{d} \cdot \sin a_{\max} (\cosh_{\max} + \cosh_{\min}). \end{aligned} \quad (3.14)$$

The result for dual frequency observations is five times as big:

$$|\delta x_3| \leq 30 \text{ mm} \cdot \frac{M_{\max}}{d} \cdot \sin a_{\max} (\cosh_{\max} + \cosh_{\min}). \quad (3.15)$$

3.3 Multipath from Nearby Objects

Multipath from nearby objects is in practice potentially more serious than ground multipath because it cannot be reduced by antenna design or absorbing material; the reflected signals may be received at the same elevation angles as the direct signals. Of

course, nearby objects can often be avoided; the ground cannot. For our purpose, the only fundamental differences between nearby objects and the ground are the facts that objects are of limited extent and arbitrary position with respect to the receiver. The geometry displayed in figure 3.2 will be applicable to many cases in practice. The y-axis is chosen parallel to the reflector surface and the reflector is horizontally symmetrical with respect to the x-axis, giving a zero bias in y-direction. The multipath region is identical to the region obstructed by the reflector as seen from the image receiver R' , where we assume for the moment that this region lies completely within the observation region.

First we need to express the limits of the multipath region in the primed system in terms of known variables. In the x-z-plane ($a = a' = 0$) we deduce from the figure that

$$h'_{\min} + h_{\max} = \alpha. \quad (3.16)$$

Consequently the limits in the primed system are

$$h'_{\min} = \alpha - h_{\max} \quad (3.17)$$

and

$$h'_{\max} = h'_{\min} + \Delta h = \alpha - h_{\max} + \Delta h \quad (3.18)$$

where we do not allow cases that yield $h'_{\max} \geq 90^\circ$. Again, these limits are really functions of azimuth a' depending on the exact shape of the reflector. We assume here that

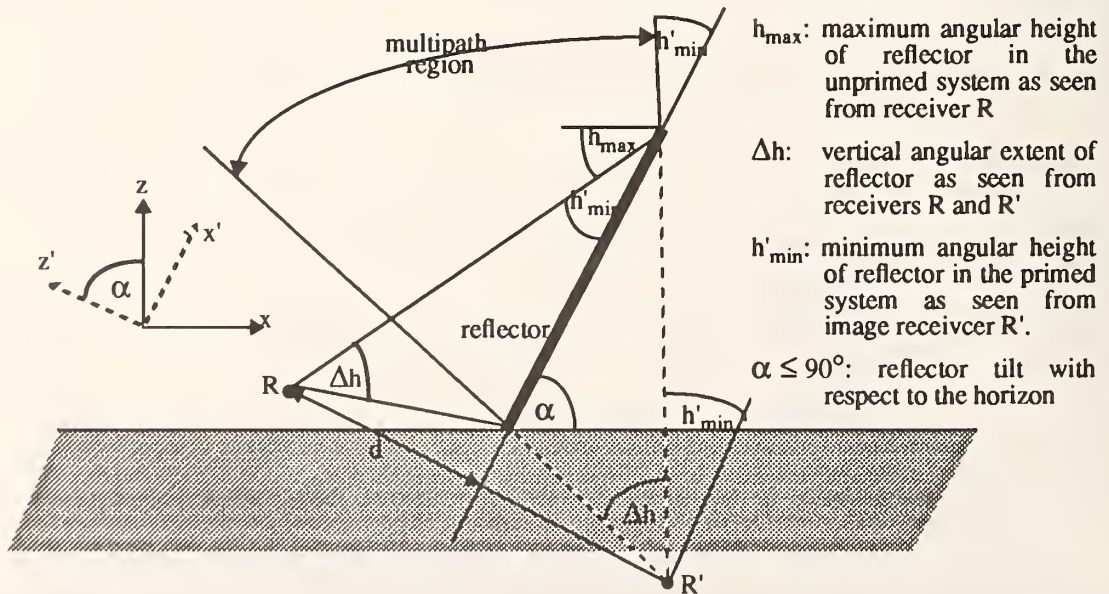


Figure 3.2. Multipath from a nearby planar reflector parallel to the y-axis, horizontally symmetrical with respect to the x-axis, and at an angle α from the horizon.

we are dealing with objects of rather limited azimuthal extent $\pm a'_{\max}$ and obtain an estimate of the integrals over the multipath region by separating the elevation and azimuthal parts in much the same way as eq (3.13):

$$\begin{aligned}
 |m'_{1x}| &\equiv \left| \int_{\text{multi}} M_1(h') \cos^2 h' \cos a' dh' da' \right| \\
 &\approx \left| \int_{h'_{\min}(a'=0)}^{h'_{\max}(a'=0)} M_1(h') \cos^2 h' dh' \int_{-a'_{\max}}^{a'_{\max}} \cos a' da' \right| \\
 &= 2 \sin a'_{\max} \cdot |I1_{xy}(h'_{\min}, h'_{\max})| \\
 &\leq 2 \sin a'_{\max} \cdot \left[\tilde{I}1_{0xy}^{\max}(\alpha - h_{\max}) + \tilde{I}1_{0xy}^{\max}(\alpha - h_{\max} + \Delta h) \right] \\
 &\leq 2 a'_{\max} \cdot 0.015 \frac{M_{\max}}{d} \cdot 2 \cos\left(\alpha - h_{\max} + \frac{\Delta h}{2}\right) \cos \frac{\Delta h}{2}, \quad (3.19)
 \end{aligned}$$

$$\begin{aligned}
 |m'_{1z}| &\equiv \left| \int_{\text{multi}} M_1(h') \cosh' \sinh' dh' da' \right| \\
 &\approx \left| \int_{h'_{\max}(a'=0)}^{h'_{\max}(a'=0)} M_1(h') \cosh' \sinh' dh' \int_{-a'_{\max}}^{a'_{\max}} da' \right| \\
 &= 2 a'_{\max} \cdot |I1_z(h'_{\min}, h'_{\max})| \\
 &\leq 2 a'_{\max} \cdot \left[\tilde{I}1_{0z}^{\max}(\alpha - h_{\max}) + \tilde{I}1_{0z}^{\max}(\alpha - h_{\max} + \Delta h) \right] \\
 &\leq 2 a'_{\max} \cdot 0.015 \frac{M_{\max}}{d} \cdot 2 \sin\left(\alpha - h_{\max} + \frac{\Delta h}{2}\right) \cos \frac{\Delta h}{2}. \quad (3.20)
 \end{aligned}$$

The transformation matrix from the primed system to the unprimed system is:

$$\mathbf{T} = \begin{bmatrix} \cos \alpha & 0 & -\sin \alpha \\ 0 & 1 & 0 \\ \sin \alpha & 0 & \cos \alpha \end{bmatrix} \quad (3.21)$$

With this we can calculate upper limits to the single-frequency bias in the x- and z-directions:

$$\begin{aligned}
|\delta x_1| &\leq \lambda_1 \cdot (|m'_{1x}| \cos \alpha + |m'_{1z}| \sin \alpha) \\
&= \lambda_1 \cdot 4a'_{\max} \cdot 0.015 \frac{M_{\max}}{d} \cos \frac{\Delta h}{2} \cdot \\
&\quad \cdot \left[\cos \alpha \cos \left(\alpha - h_{\max} + \frac{\Delta h}{2} \right) + \sin \alpha \sin \left(\alpha - h_{\max} + \frac{\Delta h}{2} \right) \right] \\
&= 11 \text{ mm} \cdot \frac{a'_{\max} M_{\max}}{d} \cos \frac{\Delta h}{2} \cos \left(h_{\max} - \frac{\Delta h}{2} \right), \tag{3.22}
\end{aligned}$$

$$\begin{aligned}
|\delta z_1| &\leq \lambda_1 \cdot 0.5 \cdot (|m'_{1x}| \sin \alpha + |m'_{1z}| \cos \alpha) \\
&= \lambda_1 \cdot 2a'_{\max} \cdot 0.015 \frac{M_{\max}}{d} \cos \frac{\Delta h}{2} \cdot \\
&\quad \cdot \left[\sin \alpha \cos \left(\alpha - h_{\max} + \frac{\Delta h}{2} \right) + \cos \alpha \sin \left(\alpha - h_{\max} + \frac{\Delta h}{2} \right) \right] \\
&= 6 \text{ mm} \cdot \frac{a'_{\max} M_{\max}}{d} \cos \frac{\Delta h}{2} \sin \left(2\alpha - h_{\max} + \frac{\Delta h}{2} \right). \tag{3.23}
\end{aligned}$$

For big angles α , i.e., near vertical reflector surfaces, the above parametrization is not valid as parts or even the whole of the potential multipath region may lie outside the observation region. Of particular interest in practice is the case of a vertical reflector as shown in figure 3.3. The total vertical angular extent of the reflector does not

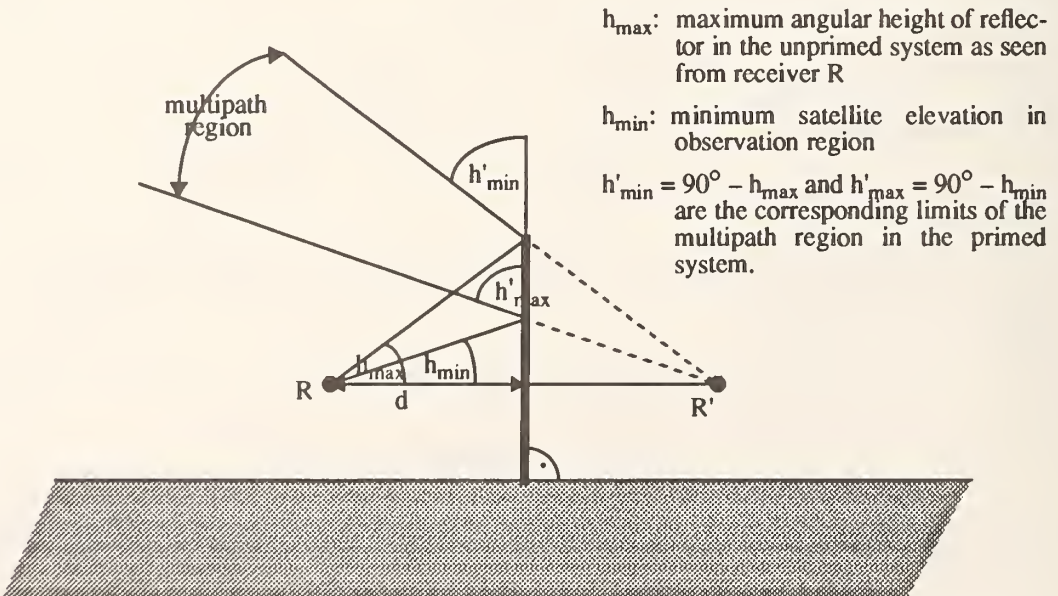


Figure 3.3. Multipath from a vertical reflector. The multipath region is determined by the angular height of the reflector h_{\max} and the minimum satellite elevation included in the fit h_{\min} .

matter now, but only the extent above the minimum satellite elevation. Hence, vertical reflectors can in principal be rendered harmless by choosing an elevation cutoff h_{\min} higher than the angular elevation h_{\max} of the reflector.

The integration limits in the primed system are now $h'_{\min} = 90^\circ - h_{\max}$ and $h'_{\max} = 90^\circ - h_{\min}$. Thus, in analogy to eqs (3.19) and (3.20):

$$\begin{aligned} |m'_{1x}| &\leq 2 \sin a'_{\max} \cdot \left[\tilde{I}1_{0xy}^{\max} \left(90^\circ - h_{\max} \right) + \tilde{I}1_{0xy}^{\max} \left(90^\circ - h_{\min} \right) \right] \\ &\leq 2 \sin a'_{\max} \cdot 0.015 \frac{M_{\max}}{d} \cdot (\sinh_{\max} + \sinh_{\min}), \end{aligned} \quad (3.24)$$

$$\begin{aligned} |m'_{1z}| &\leq 2 a'_{\max} \cdot \left[\tilde{I}1_{0z}^{\max} \left(90^\circ - h_{\max} \right) + \tilde{I}1_z^{\max} \left(90^\circ - h_{\min} \right) \right] \\ &\leq 2 a'_{\max} \cdot 0.015 \frac{M_{\max}}{d} \cdot (\cosh_{\max} + \cosh_{\min}). \end{aligned} \quad (3.25)$$

The vertical bias in the p-system is the horizontal bias in the u-system and vice versa:

$$|\delta x_1| = \lambda_1 \cdot |m'_{1z}| \leq 6 \text{ mm} \cdot \frac{M_{\max}}{d} \cdot a'_{\max} (\cosh_{\max} + \cosh_{\min}), \quad (3.26)$$

$$|\delta z_1| = \lambda_1 \cdot |m'_{1x}| \leq 6 \text{ mm} \cdot \frac{M_{\max}}{d} \cdot \sin a'_{\max} (\sinh_{\max} + \sinh_{\min}). \quad (3.27)$$

Note the analogy between eqs (3.26) and (3.14) where the bias is caused by a region of missing multipath of the same extent as the multipath region in this calculation. The corresponding estimates for dual frequency observations are again obtained by multiplying all results by a factor of five.

3.4 Multipath from Tilted Ground

As demonstrated in section 3.2, position bias due to multipath arises as a consequence of asymmetry. A relatively small disturbance of vertical angular extent $\Delta h = 2^\circ/d$ can cause the full effect. Since a perfectly flat ground is rather the exception than the rule for a receiver site, it is of interest to examine how big a horizontal bias can be introduced by a small ground tilt. Figure 2.4 illustrates the situation. The multipath region is identical to the observation region as long as the tilt is smaller than the minimum satellite elevation, which we will assume here. A horizontal bias is introduced by the ground tilt for two reasons: the vertical bias in the primed system produces a horizontal bias in the unprimed system as $\delta x = \delta z' \sin \alpha$, and the horizontal bias

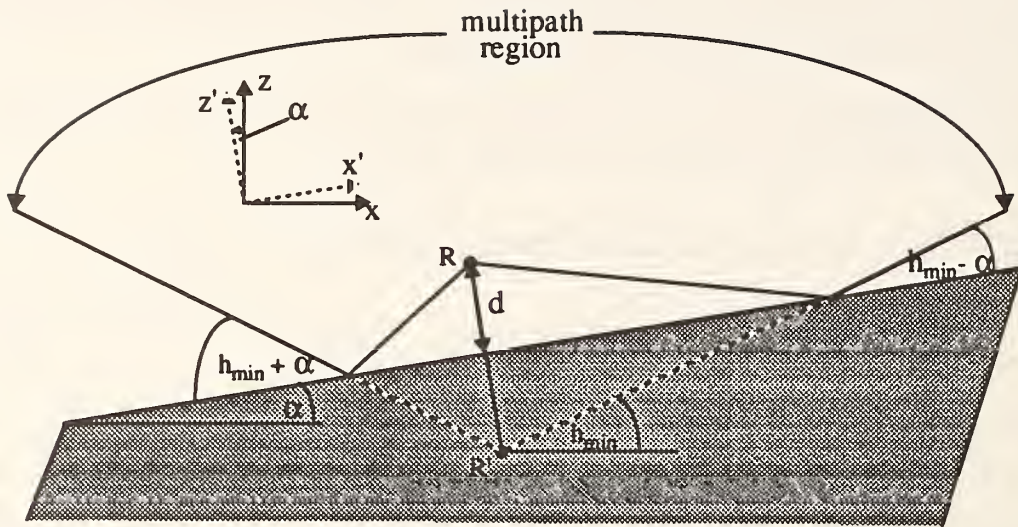


Figure 3.4. Multipath from the ground tilted at an angle α from the horizon. The multipath region is identical to the observation region.

in the primed system is non-zero because of the asymmetry of the multipath region in that system. If we assume that $\delta z'$ is of the same order as that for the flat ground calculated in section 3.2, then δx due to it becomes significant only for tilt angles greater than, say 20° . We suspect that the second reason might yield an appreciable horizontal bias for much smaller ground tilts, which shall be estimated now.

We have to evaluate the integral over the multipath region

$$m'_{1x} = \int_{\text{multi}} M_1(h') \cos^2 h' \cos a' dh' da'. \quad (3.28)$$

The method of decoupling the elevation and azimuthal integrals eq (3.13) is of no use in this case as the azimuthal extent of the multipath region is not limited; in fact, applying it would give zero as the result. We have to actually parameterize the dependencies of the limits on each other:

$$m'_{1x} = \int_0^{2\pi} \left(\int_{h'_{\min}(a')}^{90^\circ} M_1(h') \cos^2 h' dh' \right) \cos a' da'. \quad (3.29)$$

Inserting the approximated solution of the elevation integral, eq (2.42), we are confronted with

$$m'_{1x} = 0.62 \frac{M_{\max} \lambda_1}{8d} \int_0^{2\pi} \cos h'_{\min}(a') \cos \left(\frac{4\pi d}{\lambda_1} \sin h'_{\min}(a') \right) \cos a' da'. \quad (3.30)$$

It is easy to derive that, for small tilts α , the proper function of the minimum satellite elevation as a function of azimuth in the primed system is

$$h'_{\min}(a') \approx h_{\min} - \alpha \cos a'. \quad (3.31)$$

Rather than attempting to solve eq (3.30), we will now make some crude approximations and intuitive arguments that let us estimate an upper limit for it:

- (1) h'_{\min} is small, so $\cosh h'_{\min} \approx 1$ and $\sinh h'_{\min} \approx h'_{\min}$
- (2) linearize eq (3.31) in $a' \in [0, \pi]$:

$$h'_{\min}(a') \approx h_{\min} + \alpha \cdot \frac{2}{\pi} \left(a' - \frac{\pi}{2} \right) \quad (3.32)$$

- (3) the integral in eq (3.30) thus becomes

$$2 \int_0^{\pi} \cos \left[\frac{4\pi d}{\lambda_1} \left(h_{\min} + \alpha \cdot \frac{2}{\pi} \left(a' - \frac{\pi}{2} \right) \right) \right] \cos a' da' \approx 2 \int_0^{\pi} \cos(D + Fa') \cos a' da' \quad (3.33)$$

$$\text{with } D \equiv \frac{4\pi d}{\lambda_1} (h_{\min} - \alpha) \quad (3.34)$$

$$\text{and } F \equiv \frac{4\pi d}{\lambda_1} \left(\alpha \cdot \frac{2}{\pi} \right) = \frac{8d\alpha}{\lambda}. \quad (3.35)$$

Expression (3.33) reaches its maximum value of π when D is a multiple of 2π and $F = 1$. With the angles in degrees and d in m, the first condition translates to

$$0.18d(h_{\min} - \alpha) = \text{integer} \quad (3.36)$$

which is satisfied e.g., for $d = 1$ m and $h_{\min} = 20^\circ$ by $\alpha = 14.4^\circ, 8.9^\circ, 3.3^\circ$. The second condition is

$$\alpha \equiv \frac{1.4^\circ}{d}, \quad (3.37)$$

which is in fact on the order expected from the preceding sections.

Expressed in words, we have just defined conditions under which the elevation integral of figure 2.6a goes from a maximum to the next minimum while the azimuth

in the primed system goes from 0 to 180° . The horizontal bias is maximized when these conditions are satisfied. We have also found that the conditions can be satisfied for reasonable values of d , h_{\min} , and α .

Note that ground tilts smaller as well as larger than $1.4^\circ/d$ create a smaller bias. The exact solution for integral eq (3.33) is

$$2 \int_0^\pi \cos(D + Fa') \cos a' da' = \frac{4F}{1 - F^2} \cdot \cos F \frac{\pi}{2} \cdot \sin \left(D + F \frac{\pi}{2} \right) \quad (3.38)$$

which can be constrained to first order as $\leq 4F$ for small $F = 0.73\alpha d \ll 1$ and $\leq \frac{4}{F}$ for large $F \gg 1$. Both limits yield the value 4 for $F = 1$ instead of the exact value of π .

These considerations result in the following upper estimates for the horizontal bias δx_1 :

- maximum bias at $\alpha = 1.4^\circ/d$:

$$|\delta x_1| \approx |\delta x'_1| = \lambda_1 \cdot m'_{1x} \leq \lambda_1 \cdot 0.015 \frac{M_{\max}}{d} \pi \equiv 9 \text{ mm} \frac{M_{\max}}{d} \quad (3.39)$$

- for $\alpha < 1.4^\circ/d$ (α in degrees):

$$|\delta x_1| \leq \lambda_1 \cdot 0.015 \frac{M_{\max}}{d} 4 \cdot 0.73\alpha d \equiv 8 \text{ mm} \cdot \alpha M_{\max} \quad (3.40)$$

- for $\alpha > 1.4^\circ/d$ (α in degrees):

$$|\delta x_1| \leq \lambda_1 \cdot 0.015 \frac{M_{\max}}{d} \frac{4}{0.73\alpha d} \equiv 16 \text{ mm} \cdot \frac{M_{\max}}{\alpha d^2}. \quad (3.41)$$

For dual frequency observations the bias may be five times as large whenever $d \geq 20^\circ/h_{\min} \equiv 1 \text{ m}$. This limits the absolute maximum to about 10 mm. Also remember that the approximations were obtained under the assumption of a small ground tilt.

CHAPTER 4

APPLICATION OF THE MODEL

4.1 Limitations of the Applicability

Before applying the calculations of the previous chapter to the real world and specifically to the “EDM” campaign, it needs to be discussed how much the theoretical results are distorted by real world effects disregarded in the model. The fact that the object of this study, the position bias, shows a rather erratic behavior even in theory (it oscillates) already forces us to confine quantitative statements to upper limit estimates. Therefore we are now mainly concerned with the possibility that these estimates may be too small in real situations.

Let us recall the essential formulae derived for the model in Chapter 2:

$$M = \text{atan} \left[\frac{\sin\left(\frac{4\pi d}{\lambda} \mathbf{n} \cdot \hat{\mathbf{s}}\right)}{A^{-1} + \cos\left(\frac{4\pi d}{\lambda} \mathbf{n} \cdot \hat{\mathbf{s}}\right)} \right], \quad (2.6)$$

$$\delta r = -\lambda_1 \cdot \left(\int_{\text{obs}} S_o \cosh \cdot dh \cdot da \right)^{-1} \cdot \int_{\text{multi}} M \hat{s}_o \cosh \cdot dh \cdot da. \quad (2.21)$$

From this we calculated the position bias in Chapter 3 and obtained results of the form

$$|\delta r| \leq 3 \text{ mm} \cdot \frac{M_{\max}}{d} \cdot G \quad (4.1)$$

where G is a factor dependent on geometry whose components are smaller than 4π for single frequency observations. In the L3-case this result is multiplied by about five.

4.1.1 Non-uniform Satellite Distribution

If we assume for the moment that eq (2.6) gives the real error phase, the biggest shortcoming of the model is the assumption of a uniform satellite distribution in the derivation of eq (2.21). The actual satellite distribution is dependent only on the receiver site and repeats daily. The satellite elevation angles and azimuths as functions of time for the rfc station are shown in figure 4.1. While these plots are not quite the ideal means to examine the observation density in elevation and azimuth space, they do reveal the most obvious deviations from a uniform distribution, that the density decreases with increasing elevation angle; this is expected as a satellite zenith pass is a rare event. The azimuth plot displays two types of curves: those similar to inverse tangents corresponding to east-west satellite passes, and those similar to inverse tangents of the inverse argument corresponding to north-south passes. The predominance of north-south passes over North America is well known to be responsible for the better precision in the north-south direction often observed in GPS experiments if ambiguities are not resolved (e.g., [14]). Our interest here is not in the characteristics of satellite passes but only in the overall observation density throughout the session. Essentially, we imagine a horizontal grid across the angle plots and require an equal amount of data points in each row.

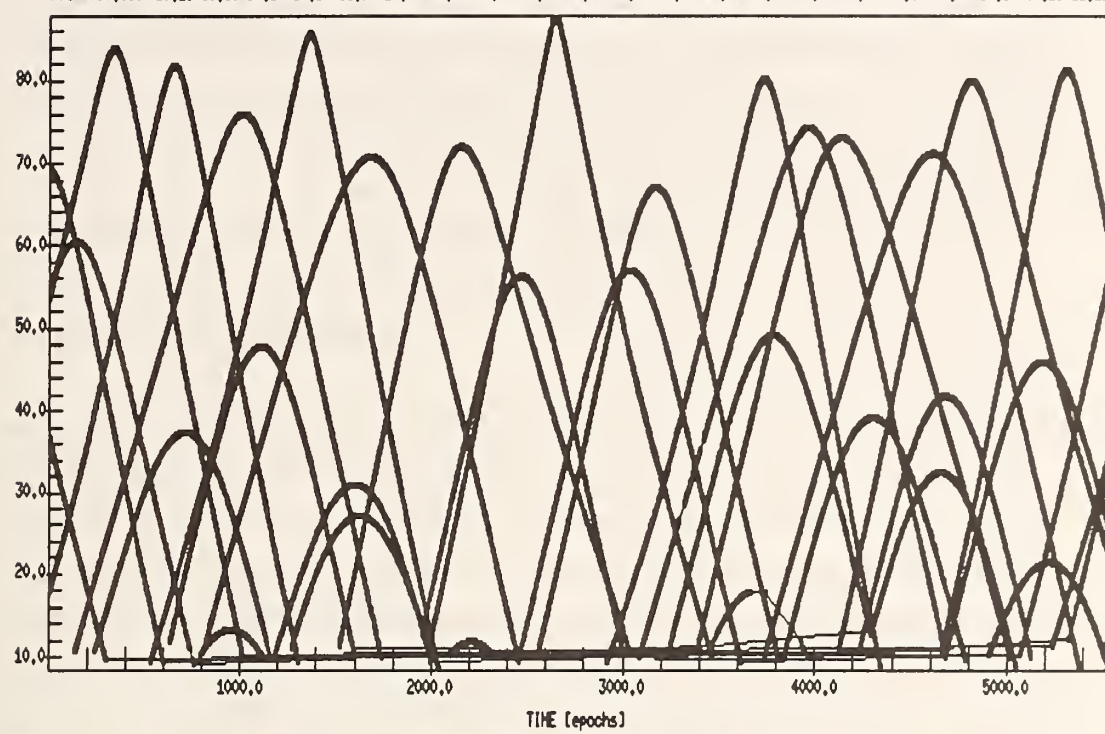
Formally, the non-uniformity of the satellite distribution would be introduced into the calculations simply as a non-constant density function $c(h, a)$ of azimuth and elevation in the integrals of eq (2.21). The real density is different from the assumed constant value in two ways:

- (1) There will be large scale variations corresponding to a systematic asymmetry depending on the receiver site. The most pronounced large-scale structure of c for almost any site is the smaller number of high elevation observations. Because both integrands in eq (2.21) are weighted by \cosh , any variability of c in the region $h \approx 90^\circ$ has little effect on the result.

To get an idea of the size of the influence, consider the extreme case of a density function that is unity for $h \leq 60^\circ$ and zero for $h > 60^\circ$. The effect on the first integral (the matrix \mathbf{B}) is rather small; it becomes the matrix

$$\mathbf{B} \cong \begin{bmatrix} 1 & 0 & 0 \\ 0 & 1 & 0 \\ 0 & 0 & 0.8 \end{bmatrix}, \quad (4.2)$$

rfcr0790_ele 29;29 18;18 14;14 25;25 22;22 19;19 28;28 27;27 11;11 16;16 02;02 15;15 26;26 13;13 12;12 24;24 20;20 03;03 17;17 23;23 21;21



rfcr0790_azi 29;29 18;18 14;14 25;25 22;22 19;19 28;28 27;27 11;11 16;16 02;02 15;15 26;26 13;13 12;12 24;24 20;20 03;03 17;17 23;23 21;21

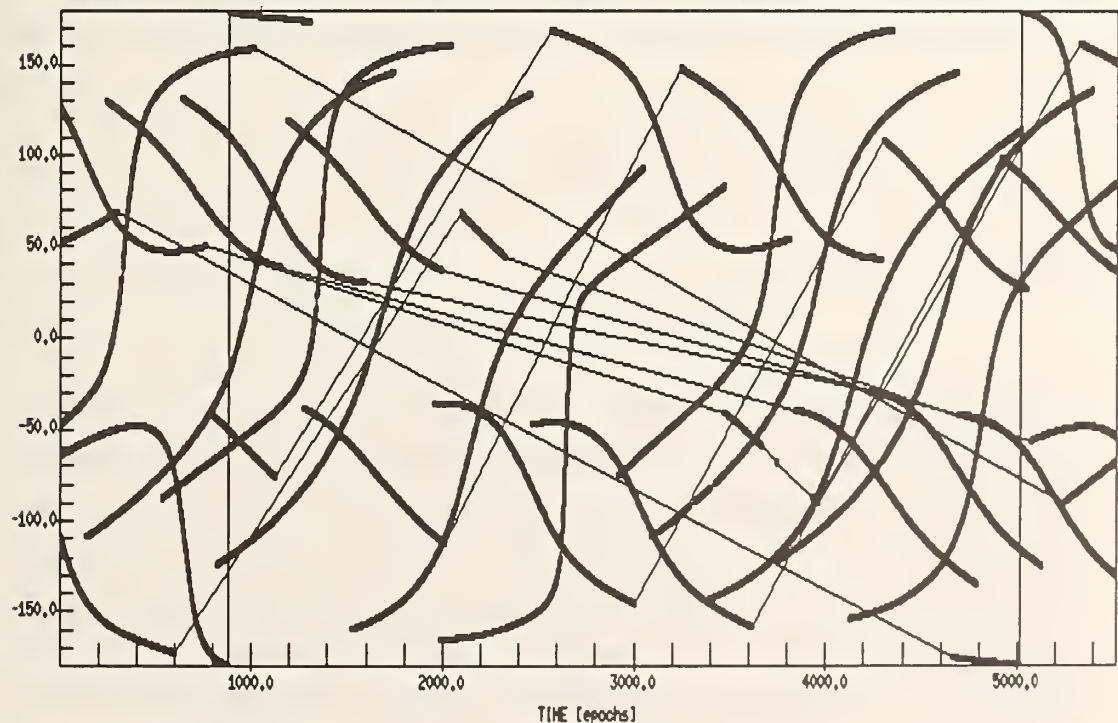


Figure 4.1. Satellite elevations (upper plot) and azimuths (lower plot) in degrees as functions of time for station rfcr. One epoch on the time axis corresponds to 15 s.

which differs from eq (2.28) only in the zz -component by about 60 percent. The second integral is only affected in cases where the multipath region extends above $h = 60^\circ$. Of course, any azimuthal non-homogeneity results in non-zero off-diagonal elements that lead, for example, to a small horizontal bias even in the case of a perfectly flat ground without obstacles.

In practice, observation times are sufficiently long to sample all directions of the sky. The large scale asymmetry is thus hardly of concern to us; it may influence the geometry factor G somewhat but will not affect the order of magnitude of our estimates given by M_{\max}/d .

(2) The density, of course, also fluctuates strongly on the small scale as the satellite orbits are discrete lines in (h, a) -space. The condition for the applicability of the model is that these fluctuations can be regarded as random for the particular receiver-reflector geometry. We could construct an extreme case of non-randomness where all observations yield the same multipath error phase so that the bias adds up instead of decreasing by averaging. This happens, for example, when all observations have an equal elevation h' above the reflector plane.

Imagine the flat ground as a reflector and satellites circling the receiver at a constant elevation h causing the (constant) error phase M . Then eq (2.21) becomes

$$\delta r = -\lambda_1 \cdot \left(\int_{\text{obs}} S_o da \right)^{-1} \cdot M \int_{\text{multi}} \hat{s}_o da \quad (4.3)$$

and thus

$$\delta z = -\lambda_1 \cdot (2\pi \sin^2 h)^{-1} \cdot M (2\pi \sinh) = \frac{\lambda_1 M}{\sinh} \quad (4.4)$$

which is independent of the distance to the reflector and could become quite big. While this hypothetical case might bear no resemblance with any real situation, the problem of non-randomness is not completely irrelevant. A satellite pass parallel to a long vertical reflector may cause an almost constant or very slowly changing error phase. If observation times are short, this particular set of observations may receive much more weight than would be predicted by our model, resulting in a larger bias. Long observation times will obviously decrease such systematic effects, but once present never completely eliminate them as no additional improvement is obtained if the observations span more than one day. It is beyond the scope of this work to quantify the influence of non-random satellite distributions on the position bias. Since general statements are hard to obtain, the

easiest way for such an evaluation would probably be a simulation using actual satellite orbit data and calculating the bias from eq (2.19). Because of the necessity of very particular geometry, situations as the one described above should be very rare. Intuitively, one would assume that the satellite distribution is sufficiently random for the model to be valid if observations include more than, say, 10 satellites, i.e., for observation times of several hours.

4.1.2 Other Unmodelled Effects

Other unmodelled effects that are of concern to us refer exclusively to the error phase, M . In chapter 2 we made the following assumptions:

Single Reflector. Multiple reflections of the same signal would occur mostly from the ground and a nearby object, whereas simultaneous reflections from two objects would be rare due to their limited extent. Thus the two reflected signals would enter the antenna from very different elevation angles (positive from the object, negative from the ground). Because of the gain pattern of the antenna, it is likely that the amplitudes differ by an order of magnitude or more, since reflection from the object prevails. It is thus a good approximation for most practical cases to calculate the error phase in a region of multiple reflections from the strongest reflection alone.

No Phase Change at Reflector. The phase difference between the direct and the multipath signal was set equal to the pathlength difference divided by the wavelength. Here we disregarded a phase change of π occurring at a conducting surface. This factor is inconsequential for the model results that employ the sinusoidal approximation eq (2.37). It will only reverse the sign of the multipath phase.

Planar Reflector. Many reflectors in practice actually are close to plane surfaces (trucks, ground, water, *etc.*). The effect of deviations from a perfect plane depend on their scale: roughness on a scale much smaller than a wavelength can be disregarded; roughness on the order of a wavelength will cause loss of the coherency of the reflected signal, i.e., the error phase will average to zero. The only case that would affect the model results would be a reflector that is bent on a scale larger than a wavelength. The whole derivation of the error phase is not applicable then, as the image receiver is not stationary and the calculated oscillation frequency becomes incorrect. The model will still be a good approximation for slight curvature.

Constant Reflection Amplitude. In reality, A varies for several reasons, most notably for the antenna gain pattern. Most modern antennas designed for high accuracy applications (among them the one used in the “EDM” experiment) feature a gain

drop between 10 and 20 dB from the zenith to the horizon, and down to 30 or even 40 dB at the backplane zenith (e.g., [15]). The amplitude of the reflected signal before entering the antenna varies as a function of incidence on the reflector (and position of the reflection point). Most importantly, reflections only occur if h' is smaller than the Brewster angle $\Theta = \arcsin \frac{1}{n}$, n being the index of refraction of the reflecting material.

The variability of the amplitude could be included in the model simply as a function of elevation and azimuth in the second integral of eq (2.21), just as the observation density in the previous section. In practice it would vary slowly, i.e., slower than the error phase itself. Therefore it would only influence the shape of the oscillation envelope of this integral and thus the geometry factor \mathbf{G} in eq (4.1). The scale of the bias, M_{\max}/d , remains correct, and we can estimate an upper limit by assuming the maximum amplitude occurring for the particular reflector.

4.2 Estimating the Amplitudes

Without question, the most important variables determining the position bias are the distance to the reflector and the maximum amplitude of the error phase. While the former is readily obtained once a reflector is identified, the latter is very difficult to model. Even if the variability as discussed in the previous section is disregarded, the calculation of the amplitude requires knowledge of the antenna gain pattern, the index of refraction, and the conductivity of the reflecting material. Needless to say, any attempt to estimate the amplitudes is subject to substantial error. As our goal here will be an upper estimate of the bias for a particular station in a particular experiment, it is probably preferable (and certainly easier) to first consult the data itself.

The postfit residuals of the double differences contain the combined noise of both stations of a baseline. This includes in the L3 case orbit errors, tropospheric errors, clock terms, and multipath noise. We will in the following section focus on two stations of the “EDM” experiment, nist and eri1: the former because its position showed unexpectedly high scatter as discussed in the first chapter; the latter because it is by all standards an extreme multipath site as will be evident below. The tactics will be the following: we compare the L3 postfit double difference residuals of the baselines containing nist and eri1 and select for each of the two the baseline and day with the smallest noise. The amplitude of the multipath noise from any reflector must be smaller than the overall noise amplitude for the particular day and, because multipath repeats daily, on any of the days. The selected plots are shown in figure 4.2, namely nisteri2 and eri2eri1, both on the first day of the experiment. Eri2 is the station with the smallest

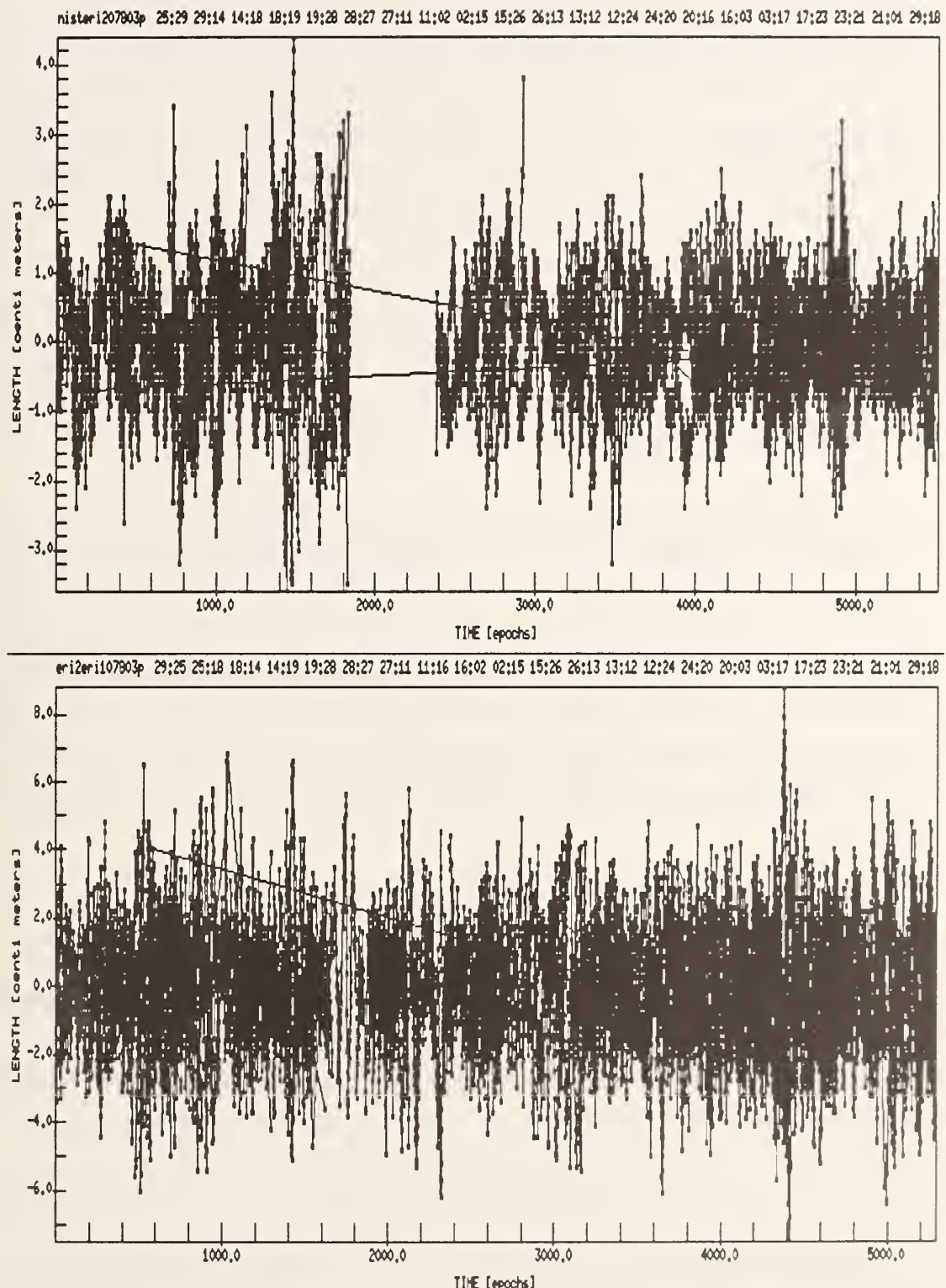


Figure 4.2. L3 postfit double difference residuals for the baselines nisteri1 (upper plot) and eri2er1 (lower plot) at day 078 (the first day of the “EDM” experiment). One epoch on the time axis corresponds to 15 s.

multipath noise (the receiver is located in an open field). From the plots we conservatively estimate a maximum multipath noise amplitude smaller than 3 cm at nist (and eri2) and smaller than 6 cm at eri1. The fact that the two Erie sites differ from each other only in their near environments also allows the conclusion that multipath at eri1 is the dominant noise source for the baseline eri2eri1. Since the amplitude of the error phase is about 4.5 times as big for L3 observations as for L1 observations (see section 2.4) we infer that

$$\text{at nist: } M_{\max} \leq \frac{3 \text{ cm}}{4.5\lambda_1} \cong 0.035 \text{ cycles} \Leftrightarrow A \leq 0.22 \quad (4.5)$$

$$\text{at eri1: } M_{\max} \leq \frac{6 \text{ cm}}{4.5\lambda_1} \cong 0.07 \text{ cycles} \Leftrightarrow A \leq 0.44. \quad (4.6)$$

At least the amplitude eq (4.6) must be quite an overestimate for reflections from the ground; the antenna gain pattern is such that the strongest ground signals (lowest elevation angle 20°) are received at a sensitivity of less than -20 dB relative to the zenith while the gain for the corresponding direct signal is about 10 dB stronger. Even for a perfectly reflecting ground the relative strength of the reflected signal must thus be smaller than 0.3. We conclude that the high amplitude at eri1 is due to reflections from several of the nearby objects. Assuming identical ground properties at the stations eri1 and eri2 we can reasonably choose eq (4.5) as upper limit for ground reflections at eri1.

4.3 Position Bias at “nist”

The environment of the nist site is drawn in figure 4.3. We consider the following causes for bias due to multipath:

Vertical Bias due to Ground Reflections. From eq (3.12) with $M_{\max} < 0.035$ and $d = 1.2 \text{ m}$ we obtain:

$$|\delta z_3| \leq \frac{60 \text{ mm} \cdot 0.035}{1.2} \cong 1.8 \text{ mm}. \quad (4.7)$$

Horizontal Bias due to Ground Reflections Plus Asymmetry Induced by the Tree. The angular height of the tree as seen from the receiver is approximately 22°, i.e., for a minimum satellite elevation of 20° the tree disturbs the symmetry of the multipath region. The tree's azimuthal extent is about 25°. Assuming that eq (3.15) derived for a flat ground approximately holds for the slight ground tilt, we thus infer

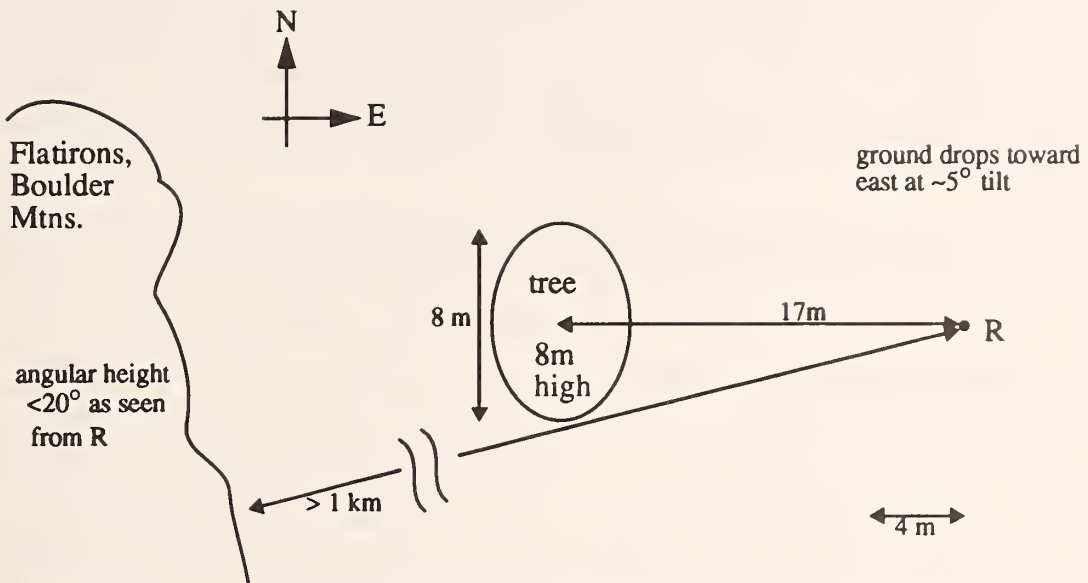


Figure 4.3. Geometry at the receiver site nist. Antenna height of R was 1.2 m above ground. All numbers given in the sketch are estimates to within about 10 percent.

$$|\delta x_3| \leq \frac{30 \text{ mm} \cdot 0.035}{1.2} \cdot \sin 25^\circ \cdot 2 \cos 20^\circ \approx 0.7 \text{ mm}. \quad (4.8)$$

Horizontal Bias due to Tilted Ground. The ground tilt in the vicinity of the receiver is about 5° . In this case $\alpha \approx 4 \times 1.4^\circ/d$, so eq (3.41) applies, yielding

$$|\delta x_3| \leq 5 \cdot 16 \text{ mm} \cdot \frac{0.035}{5 \cdot 1.2^2} \approx 0.4 \text{ mm}. \quad (4.9)$$

Horizontal Bias Induced by Reflections From the Flatirons. The Flatirons were initially suspected to be the main cause of bias. According to our model reflections off them cannot be a problem; even if the rock surface could be regarded as a plane reflector (in reality it is rough on the order of a wavelength), the error phase oscillates so fast due to the large distance that it averages out. However, this leads to a different consideration; if the reflections from the Flatirons are much stronger than the ground reflections, then they dominate the multipath phase in the region in which both reflections are present simultaneously. Hence, multipath in this region averages out, which effectively amounts to a region of missing ground multipath causing horizontal bias according to section 3.2.

We estimate the essential parameters of the Flatirons as seen from nist as follows: they are tilted at an angle of about $\alpha \approx 45^\circ$ from the horizontal, have a vertical angular

extent $\Delta h \equiv 10^\circ$, a maximum angular height $h_{\max} \equiv 20^\circ$, and an azimuthal extent $a_{\max} \equiv 30^\circ$. Simple consideration of the geometry yields that the region of missing multipath (as seen from the receiver or image receiver below the ground) lies between 80° and 90° elevation. Allowing for an error in these estimates by letting the center of this region be at 60° , we obtain from eq (3.15):

$$|\delta x_3| \leq \frac{30 \text{ mm} \cdot 0.035}{1.2} \cdot \sin 30^\circ \cdot 2 \cos 60^\circ \cong 0.4 \text{ mm}. \quad (4.10)$$

4.4 Position Bias at “eri1”

The environment of the eri1 site is drawn in figure 4.3. Here we encounter two types of multipath, from one of the nearby (vertical) objects and from the ground.

Multipath From Nearby Vertical Objects. We only have to consider objects with an angular height bigger than the minimum satellite elevation, i.e., 20° . Because of the receiver height of 1.5 m above the ground the only such objects are the meteorological tower and the trailer just south of the receiver with angular heights of 85° and 30° , respectively. The tower is neither a flat surface (but a frame of metal rods) nor close enough to cause significant bias. For the trailer, with approximate azimuthal extent in the primed system of 50° to the east and 80° to the west, eqs (3.26) and (3.27) yield

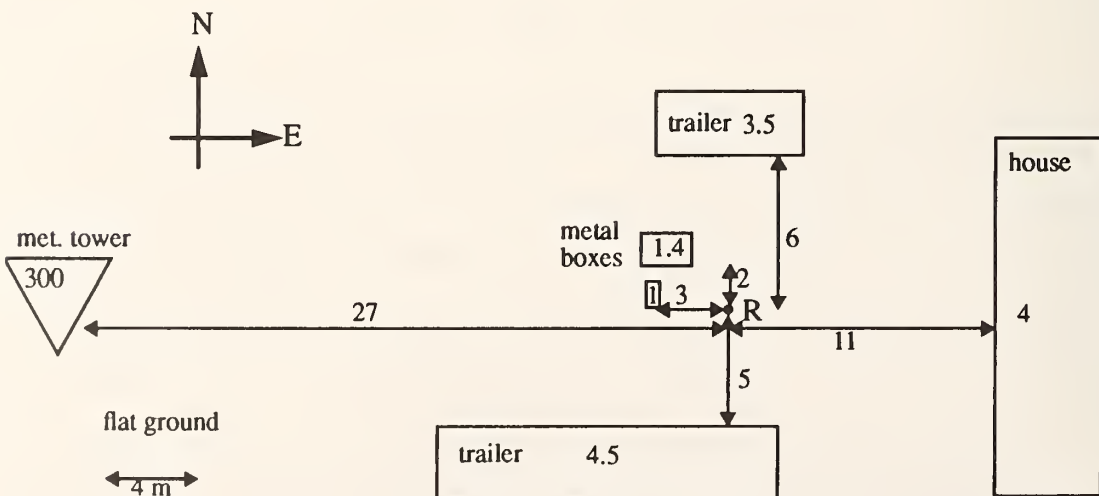


Figure 4.4. Geometry at the receiver site eri1. Numbers on arrows give the horizontal distance from the receiver in meters, numbers inside boxes give the height of objects above ground in meters. Antenna was mounted 1.5 m above ground.

$$|\delta z_3| \leq 30 \text{ mm} \cdot \frac{0.07}{5} \cdot \frac{\sin 50^\circ + \sin 80^\circ}{2} \left(\sin 20^\circ + \sin 30^\circ \right) \equiv 0.3 \text{ mm} \quad (4.11)$$

$$|\delta x_3| \leq 30 \text{ mm} \cdot \frac{0.07}{5} \cdot \frac{\pi}{180^\circ} \frac{50^\circ + 80^\circ}{2} \left(\cos 20^\circ + \cos 30^\circ \right) \equiv 0.9 \text{ mm}. \quad (4.12)$$

Hereby we slightly modified the equations to take into account the asymmetrical azimuthal extent of the trailer. Also note that because of this asymmetry, eq (4.12) is not strictly a bias in the direction of the trailer.

Multipath from the Ground. The vertical bias caused by ground reflections is similar in size as calculated above for nist (eq (4.7)), i.e., 1.8 mm, if we assume similar ground reflectivity. Horizontal bias is introduced by objects that obstruct the ground multipath region (“missing multipath”), i.e., objects with an angular height larger than 20° as seen from the image receiver 1.5 m below the ground. As is easily recognized, all objects shown in figure 4.4 qualify; we will here only calculate the largest bias that can be caused by a single object. Recalling the corresponding eq (3.15),

$$|\delta x_3| \leq 30 \text{ mm} \cdot \frac{M_{\max}}{d} \cdot \sin a_{\max} (\cosh_{\max} + \cosh_{\min}),$$

we find that the potentially most harmful objects are those of large azimuthal extent and low angular height h_{\max} (but remember that $h_{\max} - h_{\min} \geq 2^\circ/d$ is required for the full effect). The obvious candidate is again the long trailer to the south of the receiver with azimuthal extent (now in the unprimed system) of approximately 20° to the east and 70° to the west:

$$|\delta x_3| \leq 30 \text{ mm} \cdot \frac{0.035}{1.5} \cdot \frac{\sin 20^\circ + \sin 70^\circ}{2} \left(\cos 30^\circ + \cos 20^\circ \right) \equiv 0.8 \text{ mm}. \quad (4.13)$$

CHAPTER 5

SUMMARY AND CONCLUSIONS

In this work we estimate the bias on GPS position measurements caused by carrier signal multipath. While the effect is known to be severe for short observation times and kinematic GPS applications, it is expected to significantly decrease through averaging for observation times much longer than the period of multipath signatures. Typical multipath periods are on the order of several minutes while high accuracy static GPS applications usually require observations of several hours to facilitate satisfactory ambiguity resolution.

The GPS Experiment “EDM” is introduced in the first chapter. It comprised three days of observations on five receiver sites with inter-station distances between 200 m and 47 km. While the purpose of this experiment did not include testing multipath, concern over a possible multipath-induced bias arose after it was observed that site-specific length-independent error sources strongly affected at least one of the stations. Some of the summarized results show an unsatisfactorily high scatter of the shortest baseline in comparison with the longer ones. The presence of multipath signatures in the data is demonstrated as well.

A Mathematical Model of Carrier Multipath Bias is developed in Chapter 2. We first model the error phase due to multipath in terms of satellite-receiver-reflector geometry. This multipath phase is smaller than a quarter of a cycle of the carrier wavelength and oscillates with the satellite elevation angle at a frequency proportional to the reflector distance and the inverse carrier wavelength. In a second step we invoke the method of least squares to calculate the position bias from an arbitrary set of observations corrupted by multipath error. Assuming a uniform satellite distribution allows us to express the bias in terms of general geometrical parameters. The expression involves integrals of the error phase that cannot be solved analytically. We simplify in several steps: the transformation into a coordinate system in which the error phase is azimuthally symmetrical reduces the integrals to one dimension; comparison of

numerical solutions with a sinusoidal approximation and some mathematical reasoning finally lead to simple formulae that simulate the most important features of the integrals. The model is then generalized to dual frequency observations that are nowadays the standard in high accuracy applications of GPS. The main effect is a factor of about five enhancement of the maximum multipath phase amplitude.

Not surprisingly, the bias is found to be roughly proportional to the reflection amplitude, A , and inversely proportional to the perpendicular distance, d , from the reflector. Somewhat less expected is the fact that the magnitude and even the direction of the bias are very sensitive to the exact angular extent of the region in which multipath signals are received and to the distance from the reflector. The bias oscillates depending on the elevation angle above the reflector plane with a period on the order of $45^\circ\lambda/d$, i.e., for carrier wavelengths of 20 cm about $9^\circ/d[m]$. This means, for example, that the bias sign reverses if the angular extent of the multipath region changes by 5° under otherwise identical conditions. More importantly, it also implies that the bias is dependent on setup. In particular, a 10 percent change of the antenna height will reverse the sign of the bias due to ground reflections. This explains why multipath contributes to the day-to-day scatter when the setup and antenna height are varied daily as is common practice in many GPS experiments. This practice should therefore be recommended as it will allow multipath error to be represented in the repeatability rather than remaining a systematic error with unknown magnitude.

Basic Receiver Environments are examined in Chapter 3 employing the model. We obtain upper limits to the expected multipath bias in terms of the reflection amplitude, perpendicular distance from the reflector, and one or more angles characteristic of the geometry. The general rule for any geometry is that multipath bias is a product of multipath and asymmetry. Uniform multipath from all directions would in theory not cause any bias. The concept of the image receiver at an equal distance behind the (planar) reflector proves very useful within this context. To examine whether a particular environment might cause bias, all that needs be done is to identify reflectors and determine whether the multipath region as seen from the image receiver is asymmetrical.

Multipath from the flat ground causes vertical bias because it is non-symmetrical in the vertical direction (no satellites are below the ground). The azimuthal symmetry (about a vertical axis), however, precludes horizontal bias. Any azimuthal asymmetry in the field of view of an image receiver, however, introduces horizontal bias. This asymmetry could be due to any object (not necessarily a reflecting one) that obstructs a small part of the observation region of the image receiver below the ground

(corresponding to ground reflections). A reflecting surface itself effectively acts as an obstruction for the image receiver behind it. Thus, a nearby reflector will cause horizontal bias unless it is completely outside the observation region of the image receiver. Finally, an antenna placed above tilted ground results in horizontal bias because the azimuthal symmetry of ground multipath is destroyed. Of concern hereby is only the portion of ground within the observation region of the image receiver, i.e., the ground surrounding the antenna within a radius of $d/\tan 20^\circ = 2.7d$ for a satellite elevation cutoff of 20° and an antenna height d . A very small ground tilt of $1.4^\circ/d$, however, is sufficient for the maximum bias. Therefore, horizontal bias due to ground reflections can hardly be avoided despite careful site selection.

The maximum bias is of the general form and order

$$0.075 \frac{\lambda^2 M_{\max}}{d} \cdot G, \text{ i.e., } 3 \text{ mm} \frac{M_{\max}}{d \text{ [m]}} \cdot G$$

for $\lambda_1 = 19 \text{ cm}$. Here the maximum (single wavelength) error phase in cycles, $M_{\max} = a \sin A / 2\pi$, is smaller than $1/4$, and G , which is dependent on geometry, is smaller than 4π for single frequency observations and smaller than 20π for dual frequency observations. The formula is an overestimate if d is on the order of or smaller than a carrier wavelength.

These results suggest two principal ways to decrease or eliminate multipath bias:

- (1) Antenna positioning: Reflectors that could create bias must either be avoided or be distant enough to be harmless. While the ground cannot be avoided, we find that carrier multipath bias due to ground reflections is inversely proportional to the antenna height. This result appears to contradict recommendations by other authors to place the antenna as close to the ground as possible [1,15]. The argument for a very small antenna height is to yield a multipath error phase oscillating so slowly with the satellite elevation, that it remains well below the first maximum during a satellite pass. The first maximum, however, occurs at an elevation angle of approximately $2^\circ/d$, implying an antenna height smaller than about 2 cm to suppress it in a satellite zenith pass and well below that to actually reduce the bias. This can hardly be achieved in practice due to the physical dimensions of the antenna and its phase center location; one might have to place part of the antenna below the ground. We argue that a very small antenna height will likely reduce carrier multipath noise apparent in the postfit residuals, but only because the slowly varying error is absorbed by the estimated parameters and thus not visible in the adjustment residuals. This is precisely the result that is not desired. In contrast, a large antenna height will increase the multipath oscillation

frequency, preventing the error from being absorbed in the parameters for sufficiently long observation intervals. Thus the multipath signatures can be detected in the postfit residuals and the bias will be decreased by averaging over many multipath periods.

The picture is completely different for pseudorange multipath since the fundamental wavelength of the code modulations is 154 (P-code) or 1540 (C/A-code) times bigger than the carrier wavelength. Thus, pseudorange multipath error can be reduced to a small part of a cycle by placing the antenna very close to the ground. This is an effective method for minimizing the resulting bias. Note that the work presented here is not applicable to pseudorange because its signal structure and the methods to retrieve geometrical information from it are inherently different than those of the carrier signal.

- (2) Minimizing the reflection amplitude: This is usually possible only for ground reflections. Methods tested include adding absorption material or a “choke ring” to the antenna to reduce the strength of the reflected signal. Experimental tests suggest that multipath rejection measures are most effective and practical if they are designed into the antenna itself [1]. Most antennas in use for high precision measurements today feature a strongly reduced sensitivity in the backplane reducing ground multipath effects.

Application of the Model is the subject of Chapter 4. We discuss the assumption of uniform satellite distribution and unmodelled effects and conclude that the simple model is applicable to most practical situations in that it discloses the nature of multipath error and yields an upper limit estimate of its magnitude. We examine in detail the two stations of the experiment “EDM” that are thought to be most affected by multipath (nist and eri1). The reflection amplitudes are estimated from the postfit residuals. The model yields horizontal biases smaller than 1 mm and vertical biases smaller than 2 mm for all sources of multipath considered. We thus infer that even for these less than ideal receiver sites, multipath bias is essentially averaged out due to the long observation times. The remaining bias is comparable to setup errors and thus hardly a reason for concern. In any case, it cannot account for the high length-independent scatter encountered in the experiment.

Inasmuch as the conditions in the “EDM” experiment are typical for non-ideal receiver environments, we conclude that carrier multipath bias can be reduced to harmless levels by: (i) the use of antennas with a gain drop bigger than 10 dB between direct and backplane low-elevation signals (at 20°), (ii) an antenna height greater than about 1 m, (iii) no large reflective objects closer than about 5 m to the antenna, and

(iv) observation times of more than several hours. These points should be satisfied in a typical GPS campaign. The most critical issue may be the reflectivity of the ground. Note that a nearly perfectly reflecting ground would yield biases about four times as large as calculated here. In this extreme case the use of multipath suppressing devices external to the antenna would be appropriate.

Potentially more harmful than multipath bias directly induced by a carrier phase error, as examined in this work, are the effects of multipath on the data quality. Strong multipath typically gives rise to problems during data preprocessing. Fast oscillations may be misinterpreted as cycle slips by the software. Multipath can also cause loss of lock and cycle slips during the observation. Finally, multipath becomes a major limitation to the accuracy of long baselines when ambiguity resolution is attempted with the help of pseudorange information.

REFERENCES

- [1] Evans, A. G., and Hermann, B. R. A comparison of several techniques to reduce signal multipath from the Global Positioning System, in *Global Positioning System: An Overview*, edited by Y. Bock and N. Leppard, Springer-Verlag, New York, 74-81, 1990.
- [2] Meehan, T. K., Dinardo, S. J., and Young, L.E. GPS multipath reduction using absorbing backplanes, *EOS, Trans. AGU*, **70**, 1047, 1989.
- [3] Young, L.E., and Meehan, T. K., GPS multipath on code-using receivers, *EOS, Trans. AGU*, **69**, 324, 1988.
- [4] Wells, D. E., Beck, N., Delikaraoglou, D., Kleusberg, A., Krakiwsky, E. J., Lachapelle, G., Langley, R. B., Nakiboglou, M., Schwarz, K. P., Tranquilla, J. M., and Vanicek, P. *Guide to GPS Positioning*, Canadian GPS Associates, Fredericton, NB, 1986.
- [5] Georgiadou, Y., and Kleusberg, A. On carrier signal multipath effects in relative GPS positioning, *Manuscripta Geodaetica*, **13**, 172-179, 1988.
- [6] Dixon, T. H., An introduction to the Global Positioning System and some geological applications, *Rev. of Geophysics*, **29**, 249-276, 1991.
- [7] Bossler, J. D., Goad, C., and Bender, P. L. Using the Global Positioning System (GPS) for geodetic positioning, *Bull. Geod.*, **54**, 553-563, 1980.
- [8] Lichten, S. M., and Kornreich, S. Stochastic GPS estimation of tropospheric path delays, *EOS, Trans. AGU*, **68**, 1238, 1987.
- [9] Rocken, C. The Global Positioning System: A new tool for tectonic studies, *Ph.D. thesis*, University of Colorado, Boulder, 1988.
- [10] Beutler, G., Bauerisema, I., Botton, S., Gurtner, W., Rothacher, M., Schildknecht, T., Geiger, A. Atmospheric refraction and other important biases in GPS carrier phase observations, *IUGG XIX General Assembly*, Vancouver, Aug. 9-22, 1987.

- [11] Tranquilla, J. M. Multipath and imaging problems in GPS receiver antennas, *Proc. 4th Intern. Symp. Sat. Pos.*, Austin, TX, April 28 - May 2, 557-571, 1986.
- [12] Levine, J. Multiple wavelength electromagnetic distance measurements, *Geodetic Refraction*, edited by F. K. Brunner, Springer-Verlag, 45-51, 1984.
- [13] Vanicek, P., and Krakiwsky, E. *Geodesy: The concepts*, 2nd edition, Elsevier Science Publishers B.V., Amsterdam, 1986.
- [14] Larson, K. M., and Agnew, D. C. Application of the Global Positioning System to crustal deformation measurement - 1. Precision and accuracy, *J. Geophys. Res.*, **96**, 16547-16565, 1991.
- [15] Clark, T. GPS antennas: De-mystifying multipath, NASA/GSFC unpublished memo, March 5, 1992.



NIST Technical Publications

Periodical

Journal of Research of the National Institute of Standards and Technology—Reports NIST research and development in those disciplines of the physical and engineering sciences in which the Institute is active. These include physics, chemistry, engineering, mathematics, and computer sciences. Papers cover a broad range of subjects, with major emphasis on measurement methodology and the basic technology underlying standardization. Also included from time to time are survey articles on topics closely related to the Institute's technical and scientific programs. Issued six times a year.

Nonperiodicals

Monographs—Major contributions to the technical literature on various subjects related to the Institute's scientific and technical activities.

Handbooks—Recommended codes of engineering and industrial practice (including safety codes) developed in cooperation with interested industries, professional organizations, and regulatory bodies.

Special Publications—Include proceedings of conferences sponsored by NIST, NIST annual reports, and other special publications appropriate to this grouping such as wall charts, pocket cards, and bibliographies.

Applied Mathematics Series—Mathematical tables, manuals, and studies of special interest to physicists, engineers, chemists, biologists, mathematicians, computer programmers, and others engaged in scientific and technical work.

National Standard Reference Data Series—Provides quantitative data on the physical and chemical properties of materials, compiled from the world's literature and critically evaluated. Developed under a worldwide program coordinated by NIST under the authority of the National Standard Data Act (Public Law 90-396). NOTE: The Journal of Physical and Chemical Reference Data (JPCRD) is published bimonthly for NIST by the American Chemical Society (ACS) and the American Institute of Physics (AIP). Subscriptions, reprints, and supplements are available from ACS, 1155 Sixteenth St., NW, Washington, DC 20056.

Building Science Series—Disseminates technical information developed at the Institute on building materials, components, systems, and whole structures. The series presents research results, test methods, and performance criteria related to the structural and environmental functions and the durability and safety characteristics of building elements and systems.

Technical Notes—Studies or reports which are complete in themselves but restrictive in their treatment of a subject. Analogous to monographs but not so comprehensive in scope or definitive in treatment of the subject area. Often serve as a vehicle for final reports of work performed at NIST under the sponsorship of other government agencies.

Voluntary Product Standards—Developed under procedures published by the Department of Commerce in Part 10, Title 15, of the Code of Federal Regulations. The standards establish nationally recognized requirements for products, and provide all concerned interests with a basis for common understanding of the characteristics of the products. NIST administers this program in support of the efforts of private sector standardizing organizations.

Consumer Information Series—Practical information, based on NIST research and experience, covering areas of interest to the consumer. Easily understandable language and illustrations provide useful background knowledge for shopping in today's technological marketplace.

Order the above NIST publications from: Superintendent of Documents, Government Printing Office, Washington, DC 20402.

Order the following NIST publications—FIPS and NISTIRs—from the National Technical Information Service, Springfield, VA 22161.

Federal Information Processing Standards Publications (FIPS PUB)—Publications in this series collectively constitute the Federal Information Processing Standards Register. The Register serves as the official source of information in the Federal Government regarding standards issued by NIST pursuant to the Federal Property and Administrative Services Act of 1949 as amended, Public Law 89-306 (79 Stat. 1127), and as implemented by Executive Order 11717 (38 FR 12315, dated May 11, 1973) and Part 6 of Title 15 CFR (Code of Federal Regulations).

NIST Interagency Reports (NISTIR)—A special series of interim or final reports on work performed by NIST for outside sponsors (both government and non-government). In general, initial distribution is handled by the sponsor; public distribution is by the National Technical Information Service, Springfield, VA 22161, in paper copy or microfiche form.

U.S. Department of Commerce
National Institute of Standards and Technology
325 Broadway
Boulder, Colorado 80303-3328

Official Business
Penalty for Private Use, \$300